Università degli Studi di Padova

Dipartimento di Fisica e Astronomia "Galileo Galilei"

Corso di Laurea Magistrale in Astrophysics and Cosmology

Tesi di Laurea Magistrale in Astrophysics and Cosmology

HST photometry of multiple populations in the type II globular cluster NGC 6273

Laureanda
Marianna Žerajić De Giorgio

Relatore
Antonino Paolo Milone

Correlatore
Maria Vittoria Legnardi

Anno accademico 2022/2023

Index

Abstract

For a long time, the colour-magnitude diagrams (CMDs) in optical bands have been widely used for enhancing the comprehension of the globular clusters (GCs), which were considered the prototypes of simple stellar populations. More recently, the CMDs obtained from ultraviolet photometry have allowed astronomers to disentangle distinct evolutionary sequences in the GC CMDs that are associated with different stellar populations having different helium and light element abundances. Nowadays, multiple stellar populations (MPs) with different chemical compositions are common features of most Galactic GCs. Intriguingly, about 18% of the studied GCs exhibit internal variations in metallicity. These massive objects, which are called type II GCs, are considered the possible remnants of dwarf galaxies cannibalized by the Milky Way.

In this thesis, I analyzed deep multi-band Hubble Space Telescope images of the massive GC NGC 6273, which is poorly investigated in the context of MPs, due to the high amount of foreground reddening and differential reddening. I used "state-of-the-art" methods and computer programs to reduce the data and derive high-precision photometry and astrometry. Moreover, I derived a high-resolution reddening map to correct the CMD for the effects of differential reddening with unprecedented precision.

The CMDs obtained with ultraviolet and optical photometry allowed me to detect stellar populations with different metallicities along the subgiant branch and the red giant branch of NGC 6273, thus confirming the previous conclusion based on spectroscopy that NGC 6273 is a type II GC.

In addition, through the construction of a chromosome map relative to the RGB I could verify the presence of two main populations with different metallicity and quantify the metal-rich stars, that result to be the 40%.

I also derived an accurate determination of the RGB width in the pseudo-colour $C_{F336W,F438W,F814W}$, which is a proxy of the maximum internal star-to-star elemental variation. The finding of a wide RGB in NGC 6273, when compared with results from a large sample of GCs, corroborates the conclusion that the complexity of GC

stellar populations, including the nitrogen and helium variations, mainly depends on cluster mass.

Moreover, I identified for the first time multiple populations with different metallicity along the asymptotic giant branch (AGB) finding that the metal-rich stars are the 9% of the total number of stars, thus discovering a lack of metal-rich AGB stars similar to what is observed in other type II GCs. This finding suggests that the metal-rich stars skip the AGB phase, thus evolving as AGB manqué stars, possibly due to their extreme helium content.

1. Introduction

Globular clusters (GCs) are spheroidal ensembles of stars that orbit a galaxy such as the Milky Way. The Galactic GCs are ancient stellar systems with ages between 12 and 14 billion years (e. g. Dotter et al. 2010, Vandenberg et al. 2014).

Hence, they are among the oldest objects in Universe, and possibly the oldest objects for which reliable age determinations can be inferred from photometry. This fact makes globular clusters important tools to study the formation of the Galaxy in the early Universe and its evolution.

1.1 Multiple stellar populations

Historically globular clusters were considered the best example of old simple stellar populations, that is an assembly of coeval and chemically homogeneous single stars (e. g. Renzini & Buzzoni 1986). This conclusion is based on the colour-magnitude diagrams (CMDs) that were available in the past, where all the stars distribute along a single sequence, thus resembling a single isochrone.

Recent studies have enlightened that the colour-magnitude diagrams of GCs are composed of distinct stellar sequences that can be traced along the main evolutionary stages. Each sequence is composed of stars with different chemical properties and with significant chemical abundance spreads within them, which are considered as the signature of hydrogen burning process at high temperatures.

These photometric and spectroscopic features of GC stars, which are observed in nearly all Galactic GCs, are indicated as multiple stellar population (MPs) phenomenon.

GCs typically host two main stellar populations. A group of stars that share a similar chemical composition as field stars with same metallicity, and stars characterized by chemical abundances that are rarely found in the field and are not present in open

clusters. These stars with "anomalous chemistry" are a distinctive feature of GCs (see Bastian & Lardo 2018, Gratton et al. 2019, Milone & Marino 2022 for recent reviews).

Specifically, the first generation (1G or 1P) includes stars having the same light elements abundance as the field stars with similar metallicity, namely the primordial chemical composition (O-rich, Na-poor), while the second generation (2G or 2P) would include those enhanced in He, N, Na, Al and in some cases Mg, Si, K, and depleted in C, O with respect to the field ones with the same [Fe/H]. The variations in these light elements set well-defined chemical patterns, such as the O–Na, C–N, Mg–Al anticorrelations (see example in figure 1.2) and Na–N, C–O correlations, meaning that the 1G stars preserved the chemical composition of the pristine material (oxygen-rich, sodium-poor) from which they formed while the 2G underwent an enrichment by a process which still needs to be clarified, but which is possibly linked to the presence of chemical elements that are produced via the CNO cycle.

However, while oxygen can be potentially depleted inside low-mass stars through the CNO cycle reactions, variations in the abundances of heavier elements like Na, Al and Mg could not be produced by fusion reactions within low-mass stars, because their temperatures are too low in order to activate the chains of Ne, Na and Mg, Al of the p-capture reactions. This implies that the abundance anomalies are most likely produced internally to massive stars.

Imaging allows us to discriminate between 1P and 2P through photometry in samples composed of many thousands of stars, while simultaneously covering a wider region in the sky with respect to spectroscopic methods. Splits or spreads in cluster CMDs have been used to identify MPs and constrain their properties. The cause of these features depends on the colour or colour combinations used to image clusters and on the specific evolutionary stage considered.

A summary of the main photometric tools that are effective to maximize the separation between stellar populations with different chemical composition is the following:

✓ CMDs made with U-band photometry are powerful to identify multiple stellar populations along different evolutionary phases. Indeed stars with different abundances of C, N, O, Na define distinct red giant branch (RGB) sequences in the U vs. U–B colour-magnitude diagram, with 2P stars that exhibit fainter U magnitudes and redder U–B colours than 1P stars as a result of their enhanced nitrogen and depleted carbon abundances.
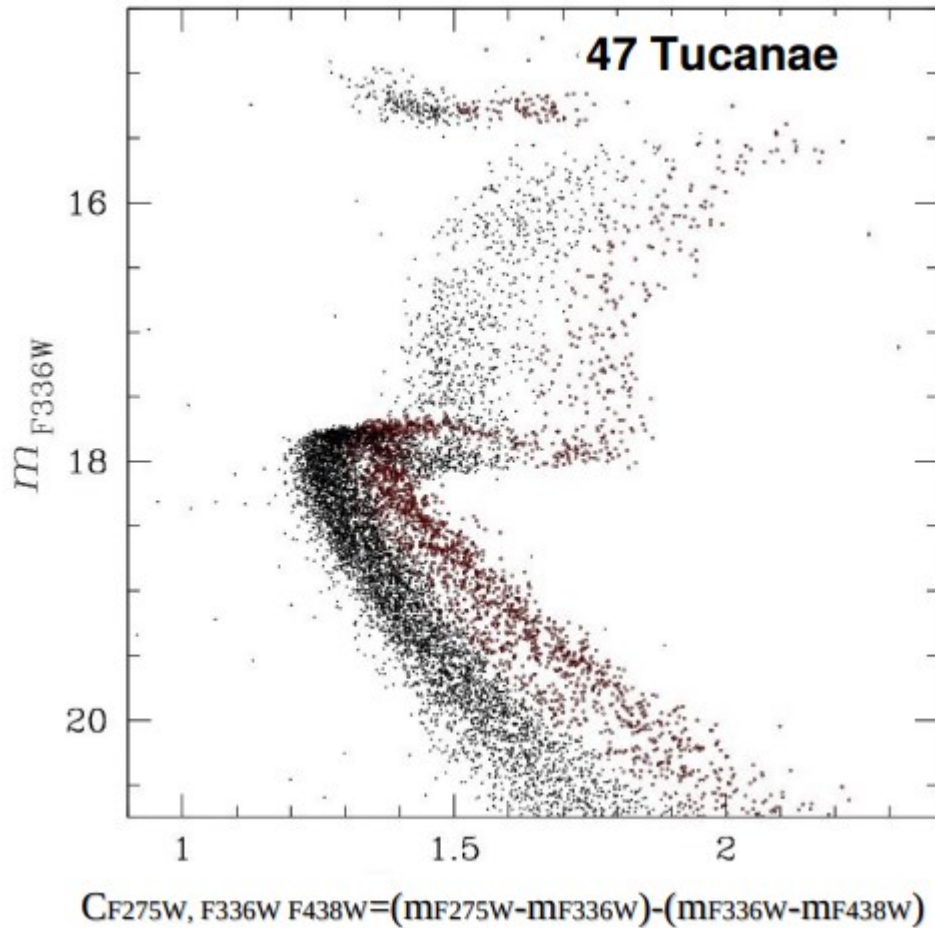
Figure 1.1 Photometric diagram of the GC 47 Tucanae where we can clearly discern different stellar populations along the evolutionary sequences (Milone et al. 2013).

✓ Stellar models predict that main sequence (MS) and RGB stars with different He contents but the same luminosity have different effective temperatures. Hence He-rich stars exhibit bluer colours than stars with pristine He abundance ($Y\sim0.25$). Wide colour baselines are more sensitive to helium variations than colours made with optical filters, thus allowing to disentangle stellar populations with small helium differences of $\Delta Y=0.01$ or less (Milone et al. 2012). In particular, since 2P stars are He-enhanced with respect to the 1P, they have bluer colours than 1G stars at the same luminosity.

✓ Near-infrared photometry is an efficient tool to identify multiple populations of M dwarfs, for example employing bands that are affected by absorption from
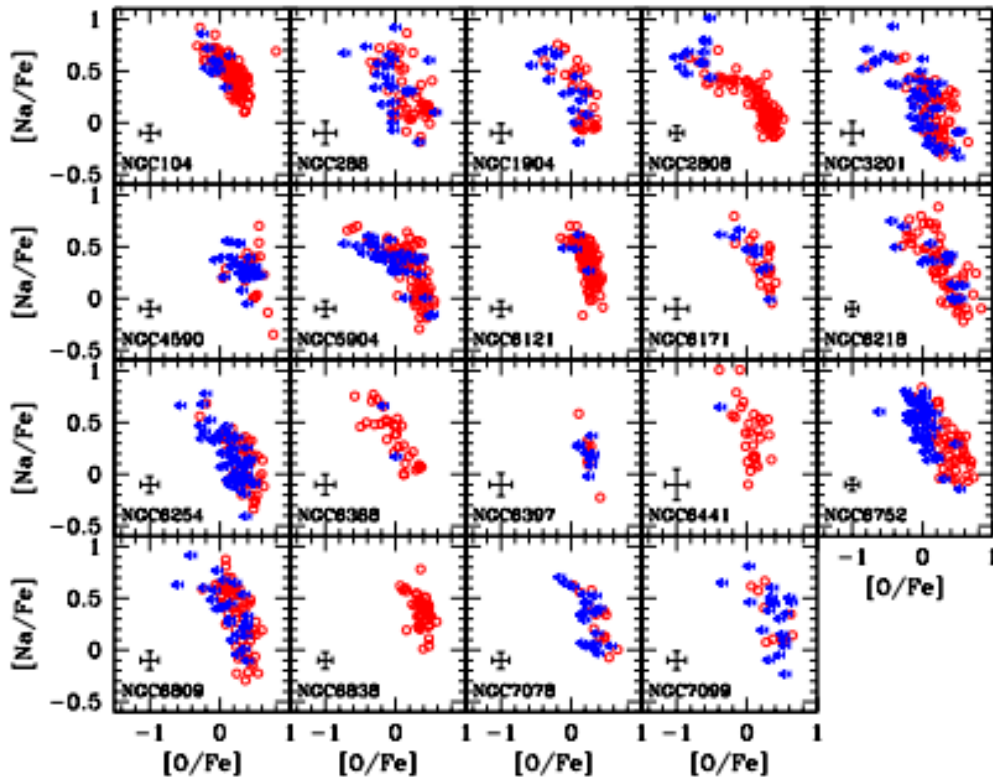
Figure 1.2 Na–O anticorrelations of 19 globular clusters. Upper limits in O abundances are shown as blue arrows, detections are indicated as red open circles (Carretta et al. 2009).

molecules that contain oxygen, and since 2P stars are O-depleted they will have brighter magnitudes than the 1P.

✓ Two-colour diagrams involving far-UV, UV and optical filters are widely used to identify multiple populations along different evolutionary phases, with the two populations being alternatively brighter or fainter according to the combination of filters. Another possibility to investigate MPs is to combine colours to define pseudo-colours, for example involving the three filters on board the Hubble Space Telescope F275W, F336W and F438W (from ultraviolet to optical): $C_{F275W,F336W,F438W} = (m_{F275W}–m_{F336W}) – (m_{F336W}–m_{F438W})$.

✓ The photometric diagram named *chromosome map* (ChM) is a pseudo-two-colour diagram that is built for MS, RGB or AGB (asymptotic giant branch) separately. The main difference with a simple two-colour diagram is that the sequences of stars are verticalized in both dimensions in such a way that stars of each stellar population are clustered in a restricted area of the ChM. The ChM is

derived from colours that are sensitive to the specific composition of GC stars with the aim of maximizing the separation among the distinct populations.

✓ Variations of He between 1P and 2P stellar groups may also affect the colour and luminosity of the RGB bump (Bragaglia et al. 2010), so the magnitude differences between the RGB bumps of the two populations from multiband photometry can be used to constrain their relative helium content (Lagioia et al. 2018).

In the past years, astronomers developed various scenarios to explain the formation of multiple populations in GCs (see Renzini et al. 2015 for a critical review). Currently, these scenarios are divided into two main groups. One in which GCs have experienced multiple bursts of star formation such that they host multiple generations of stars. In this case the CNO-processed material ejected by a first generations of massive stars polluted the intra cluster medium, out of which successive generations of stars were born. Since the second generation represents the majority of present-day GC stars, the implication of this scenario is that GCs were much more massive at the epoch of formation by a factor of ten or even more and they lost most of their 1P stars thus providing a significant contribution to the assembly of the Galaxy and the reionization of the universe (e. g. Renzini 2017).

The alternative scenario of formation concerns a single generation of coeval stars such that multiple sequences are the product of accretion of polluted material belonging to massive pre-main sequence stars of the same generation. The main candidate polluters are supermassive stars (Gieles et al. 2018) or massive binaries (Bastian et al. 2013).

A constraint on the progenitors is that the majority of globular clusters show a sum of the abundances of the C, N and O elements (C+N+O) that is constant, which means that these stars ought to start the CNO cycle at high temperatures ($T \gtrsim 10^7 \ K$) but not the helium burning ($T \gtrsim 10^8 \ K$).

The most accredited types of progenitors, in short, are:

✓ Intermediate-mass asymptotic giant branch stars

This scenario predicts that there was an initial star formation event that produced 1P stars and when they experienced the AGB phase, their ejecta expelled through slow stellar winds were retained inside the cluster potential well polluting the interstellar medium. Then in the centre of the cluster, where the AGB ejecta together with the pristine material accumulated via cooling-flow, successive generation of stars formed (e. g. Ventura et al. 2003, D'Antona et al. 2016).

- ✓ Fast-rotating massive stars

  These stars rotate near a critical velocity that is the velocity at the equator for which the centrifugal acceleration balances the gravity. The products of their phase of hot hydrogen burning are carried up to the stellar surface as a result of the mixing induced by rotation and they gradually lose mass through slow equatorial winds creating a Keplerian disk, from which the formation of 2P stars occurs (e. g. Decressin et al. 2007).

- ✓ Massive interacting binaries

  Also binary systems of massive stars could be the sources of the material from which the second generation was born, through stellar ejecta originating from the interaction and retained within the potential well of the proto globular cluster. Then 2P stars would subsequently form from the polluted material diluted with the pristine gas (De Mink et al. 2009).

- ✓ Super-massive stars

  Stars exceeding masses of 10^3 $M_\odot$ could be responsible for the pollution of the gas from which 2P stars formed. They would sink towards the centre of the cluster due to dynamic friction and once there they would experience coalescence, forming a super-massive star which during its evolution loses a significant amount of mass as a result of instabilities and stellar winds. This material is enriched in He, in the products of CNO cycle and p-capture reactions, and mixing with the original material would form the 2P stars (Denissenkov et al. 2013).

One more intriguing fact on multiple populations phenomenon is that there is a significant anticorrelation between the fraction of 1P stars and the mass of the host cluster, with massive GCs hosting a smaller fraction of these stars while the fraction of 2P stars increases with the cluster mass. Hence the multiple population phenomenon appears to systematically increase in incidence and complexity with increasing cluster mass.

1.2 Type II globular clusters

The chromosome maps, which are now available for a large sample of about 70 GCs, allow us to constrain the abundances of various chemical elements for a large number of GC stars. Indeed, the position of stars in these diagrams is particularly sensitive to the abundance of C, N, O, Mg elements via the molecules they form and to helium. This way we can separate stellar populations, and thanks to this tool astronomers have discovered that the Galaxy hosts two types of globular clusters, with distinct photometric and spectroscopic properties.

The majority of Milky Way GCs (about the 82% of the studied GCs) belongs to a first class, named *type I*, with ChMs populated by two major, well-separated groups of stars that we identify with the first population and the second population, with similar metallicity but different abundances of some light elements as described in the previous paragraph.

As illustrated in the left panel of figure 1.3, where I show the ChM of NGC 6723, 1P stars are distributed around the origin of the ChM and span a narrow range of $\Delta_{C\_F275W,F336W,F438W}$ values. The group of 2P stars that includes the remaining RGB stars spans a wide range of both $\Delta_{C\_F275W,F336W,F438W}$ and $\Delta_{F275W,F814W}$ values.

The second class, defined *type II* globular clusters, is constituted by 18% of the clusters studied through the chromosome maps and are characterized by a more complex pattern where both 1P and 2P sequences appear to be split, creating more subgroups or streams. In particular they show one or more additional sequences on the ChM besides the 1P and 2P ones, placed on the red side of the map and constituted by Fe-richer stars (figure 1.3, right panel). These clusters are spectroscopically classified as "anomalous", that is GCs exhibiting internal variations not only in light elements involved in H-burning processes, but also an enrichment in heavier elements, specifically those produced via slow neutron-capture reactions (even if observations suggest that metals and s-elements enrichment are not coupled with each other), and can be identified by the following properties:

✓ a dispersion in metallicity [Fe/H] exceeding ~0.10 dex,
✓ multiple photometric sequences, even more than two,
✓ a significant abundance spread for light elements and also heavy elements produced by the s-process,

✓ split or broad subgiant (SGB) and red giant branches in the colour-magnitude diagrams, since the faint part of the SGB evolves into a distinct RGB sequence with redder *U–I* colours. Stars on the red part of the RGB also define distinct sequences along the asymptotic giant branch and the horizontal branch (HB).

All type II clusters exhibit either split or multimodal subgiant branches when observed in both ultraviolet and optical filters, with the fainter SGB joining into the red RGB populated by stars with enhanced heavy element abundance, in contrast to type I GCs where MPs along the SGB are visible only in CMDs that include ultraviolet bands (Milone et al. 2008, Marino et al. 2009, Piotto et al. 2012).

The fraction of red RGB stars with respect to the total number of RGB stars differs significantly from one type II cluster to another, ranging from a minimum of ~4% to a maximum of ~64%, coming almost to dominate the cluster (Milone et al. 2017).

The s-process enrichment is observed in a significant fraction of anomalous GCs, suggesting that, even if the range in metallicity variations is different in these objects, they have experienced some contribution from low-mass AGBs. Fe and *s* enrichments are very likely due to different mass ranges and polluters, e. g. to high-mass and low-mass 1G stars, respectively. A possibility is that in these more massive proto-clusters the star formation proceeded for longer times than in normal clusters, giving the possibility to low-mass AGBs to contribute to the enrichment of the proto-cluster. At the time these low-mass stars started to pollute the intracluster medium, material enriched from fast supernovae may have had the time to undergo fall-back into the cluster.

Type II globular clusters are among the most massive GCs of the Milky Way, suggesting that high cluster mass is required to generate their metal-rich stellar populations. In addition, the more massive the GC is, the higher is the amount of iron that has been incorporated in the red anomalous stellar population on the ChM (Marino et al. 2021).

The variations in the overall metallicity were considered a peculiarity of more massive stellar systems such as galaxies, which are capable of retaining supernovae ejecta differently than normal globular clusters. Thus, the complex chemical pattern of these anomalous objects has introduced the idea that they could have originated in extra-Galactic environments, being the remnants of now disrupted dwarf galaxies. Such dwarf galaxy environment could explain the capability of these GCs to support more extended star formation episodes than typical GCs, which show variations in light elements only.

Additional support for the idea that the anomalous GCs may constitute the central remnants of dwarf galaxies after the outer layers have been stripped away comes from observations, for example of the GC M54, whose position coincides with the nucleus of the Sagittarius dwarf galaxy (Layden & Sarajedini 2000) and has metallicity variations (Carretta et al. 2010). Also, a low-density halo of stars surrounding NGC 1851 has been discovered by Olszewski et al. (2009), with a s-poor chemistry, and the absence of s-rich stars in this halo may suggest either that this GC is losing s-poor stars into the field, or that this sparse structure is the remnant of a dwarf galaxy, as its composition is compatible with field stars at similar metallicity.

An example of type II cluster is ω Centauri, a massive globular cluster ($\log(M/M_\odot)$ = 6.4, Milone et al. 2017) which exhibits considerable internal variations of many light elements (He, C, N, O, Na, Mg, Al, Si, K, and an enhancement in the C+N+O abundance) and also of s-elements, with extreme Fe spread (about 1.5 dex, Marino et al. 2012). It is a consolidated hypothesis the fact that it is the surviving nucleus of a dwarf galaxy, with evidence of tidal debris. The colour-magnitude diagram of ω Centauri shows multiple sequences along all the evolutionary stages, from the main sequence to an extended multimodal horizontal branch, through a complex multiple subgiant branch, but what is unique for this cluster is the complexity of its multiple populations as one can infer from its chromosome map (figure 1.4), with a number of stellar populations estimated around 16 or even more.

1.3 Asymptotic giant branch stars

The asymptotic giant branch is a brief but important phase pertaining to low and intermediate mass stars ($3\ M_\odot \lesssim M \lesssim 8\ M_\odot$) and starts at the exhaustion of helium in the centre, thus subsequently to the horizontal branch phase, which is in turn subsequent to the red giant phase. It begins when stars reach the condition of a degenerate core made of carbon and oxygen, while the helium burning shifts to a shell around the CO core. It is site of rich nucleosynthesis.

Initially in the so-called *early AGB phase* (EAGB), after the exhaustion of helium in the centre, all layers below the H-burning shell contract until He burning shifts to a
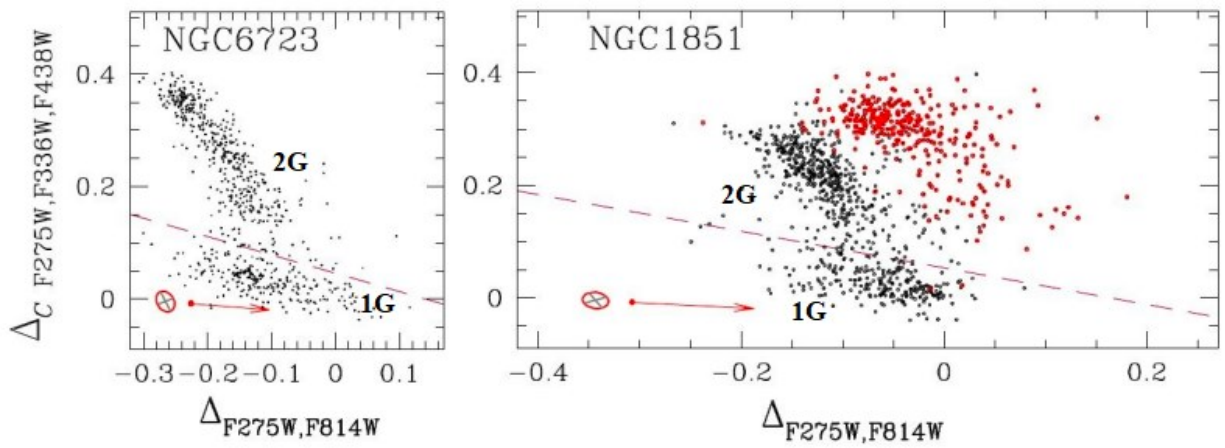
Figure 1.3 Comparison of chromosome maps of two globular clusters, type I on the left (~82% of GCs), type II on the right (~18% of GCs). Red dots mark the red RGB stars (Milone et al. 2017).
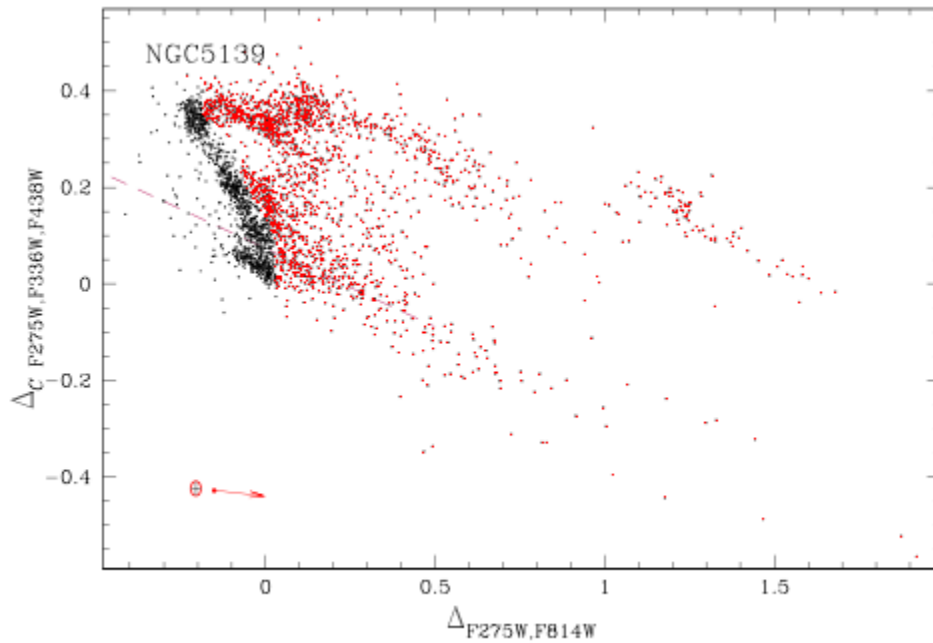

Figure 1.4 The complex chromosome map of type II GC ω Centauri. The magenta dashed line is used to separate bona fide 1G from 2G stars, red points indicate red RGB stars and the arrow indicates the reddening vector (the plot uses photometric data corrected for differential reddening, Milone et al. 2017).

shell around the core made of carbon and oxygen. The star has now two active shells, which cause the core to contract, the He-rich layers above to expand and the outer envelope to contract. Due to the expansion of the He-rich zone, the temperature in the H-shell decreases and the H-burning shell is extinguished, causing this zone plus the H-rich outer envelope to expand in response to the core contraction. During this EAGB phase the effective temperature of stars decreases while the luminosity, mainly provided by the He-shell burning, increases, until they asymptotically reach the near red giant branch.

The He-burning shell adds mass to the growing CO core which finally becomes degenerate. In stars of mass $M \gtrsim 4\,M_\odot$, as the process continues, the convective envelope penetrates deeper until it reaches the discontinuity left by the extinct H-shell, and an episode of dredge-up can occur. For lower-mass stars the H-burning shell remains active at a lower level, which prevents the convective envelope from penetrating deeper into the star, and the dredge-up does not occur. In the layers that undergo this process, hydrogen has been burned into helium, and C and O have been converted into N via the CNO cycle. This material is mixed with the outer envelope and appears at the surface.

After the EAGB, another phase of double shell burning begins, but the shells do not burn at the same pace: the He-burning one becomes thermally unstable and undergoes periodic thermal pulses. This phase is the *thermally pulsing AGB* (TP-AGB), and is characterized by some peculiar properties:

✓ the thermal pulses alternate with mixing episodes giving rise to an important phenomenon of nucleosynthesis, producing especially C, N and elements heavier than iron,

✓ the envelope is gradually eroded by strong stellar wind, which forms a dusty circumstellar envelope out to hundreds of stellar radii,

✓ the extended stellar atmosphere and circumstellar envelope have a rich molecular and dusty chemistry, as revealed by their infrared spectra,

✓ the outer convective envelope can descend beyond the H shell such that material from the intershell region is mixed into the outer envelope, originating one more episode of dredge-up.

The main effect of thermal pulses and dredge-up is the appearance of helium burning products at the surface, in particular carbon.

AGB stars are considered the major producers in the Universe of carbon, nitrogen and elements heavier than iron. These last are created via the slow neutron capture reactions (s-process) on Fe nuclei, and are elements such as Zr, Y, Sr, Tc, Ba, La, Pb.

The synthesis of s-process elements requires a source of free neutrons, which can be produced in the He-rich intershell region by the He-burning reactions, and then the carbon and s-process material are mixed into the surface in the following dredge-up phase.

In stars of mass $M \gtrsim 4\,M_\odot$, the temperature at the base of the convective envelope during the interpulse period becomes high enough ($T \gtrsim 3 \times 10^7\,K$) so that the CNO cycle takes place operating on material in the convective envelope through a process called *hot bottom burning*, which main effects are an increase in the surface luminosity and the conversion of the dredged-up C into N. Other nuclei produced during hot bottom burning are Li, Na, and isotopes of Mg.

The final evolution of AGB stars is determined by the rate of mass loss through stellar wind, which causes the loss of more or less great part of the hydrogen envelope, and finally, when also the H-burning shell is extinguished, the degenerate CO core left cools as a white dwarf.

The AGB evolutionary timescale is about 10 times faster than that of RGB stars brighter than HB stars, which involves that only through a limited number of globular clusters we can obtain a detailed investigation on multiple populations in this evolutionary phase.

1.4 Multiple populations along the AGB

Currently the most relevant studies about multiple populations come from the analysis of photometric and spectroscopic properties of main sequence stars and red giant stars, while later evolutionary phases are more complex to investigate. In the case of the horizontal branch the age-metallicity and helium mass-loss degeneracy prevent a proper understanding of the consequences that chemical variations have on the colour distribution of core He-burning stars in CMDs, and this indetermination propagates to the successive stage, the AGB, where the uncertainty on the subpopulation distribution is amplified also by statistical fluctuations due to the fast evolutionary timescale.

The AGB sequences of ~25% of the studied globular clusters show lower fractions of 2P stars than the RGBs, and only the 2P stars with an extreme chemical composition, namely those highly enhanced in helium, seem to skip the AGB phase. Indeed hot horizontal branch stars with tiny hydrogen atmospheres, usually associated with the most He-rich old stellar populations, having too small envelope mass would avoid the early AGB, characterized, as we have seen, by a gradual expansion and cooling of the star envelope, and would instead evolve to higher temperatures and luminosities, directly reaching the white dwarf cooling sequence. Thus the shell helium-burning phase of these stars is called *AGB manqué*, the major difference between AGB manqué and normal AGB stars being the core mass within the hydrogen-helium discontinuity.

However simulations of CMDs show that He variations alone could not be enough to explain the lack of AGB stars with extreme chemical composition, so the presence of AGB manqué stars in these clusters may imply that their 2P stars lost significant amount of mass in the RGB phase compared to the 1P ones.

Another recent discovery concerns some type II globular clusters where, once differentiating AGB stars of the metal-poor and metal-rich populations, it was found that AGB to RGB ratios are significantly smaller among metal-rich stars than in the other class, but the physical explanation of this phenomenon is still unknown.

1.5 Thesis layout

In this thesis I will derive the colour-magnitude diagrams of the globular cluster NGC 6273 combining magnitudes in different bands of the ultraviolet, optical and near-infrared. I will also correct them for differential reddening. The analysis will then focus in particular on multiple stellar populations along the asymptotic giant branch stars in this type II globular cluster.

The chapters are structured as follows: in this first chapter I introduced the various elements of my analysis: multiple stellar populations, type II globular clusters and asymptotic giant branch stars; the second chapter describes the dataset I collected and the methods I applied to reduce it, obtaining the final catalog also corrected for differential reddening; in the third chapter I analyze the photometric diagrams

(colour-magnitude, pseudo-colour, chromosome map) I developed basing on the final photometric values of the previous section, focusing in particular on those where we can visually distinguish multiple populations, in order to accomplish the measurement of the width of the red giant branch, which will turn out to be an important parameter regarding MPs, and the identification of normal and anomalous AGB stars; in the fourth and last chapter I summarize the global results of my work drawing the conclusions.

2. Data reduction

2.1 Target: NGC 6273

My analysis is based on NGC 6273, a crowded globular cluster near the Galactic bulge. It is one of the most massive and luminous clusters in the Galaxy, with a mass M ~ 1.2×10^6 M$_\odot$ and an absolute magnitude $M_V = -9.13$ (Harris 1996; Brown

NGC 6273 (*SIMBAD*)	
α	$17^h\ 02^m\ 37.69^s$
δ	-26° 16' 04.6''

et al. 2010), and one of the most elliptical, $\varepsilon = 0.28$ (Harris et al. 1976; Djorgovski 1993).

It is placed at a Galactocentric distance of 0.7 kpc and a height above the plane of 1.4 kpc (Casetti-Dinescu et al. 2010), belonging to the inner Galaxy globular cluster population. The distance from the Sun is ~9 kpc (Piotto et al., 1999).

It is subjected to significant differential reddening.

The colour spreads observed by Piotto et al. (1999) and Rutledge et al. (1997) provided the first evidence that NGC 6273 hosts stars with different metallicities. More recently, high-resolution spectroscopic measurements from Johnson et al. (2015b) showed that the cluster contains stars with [Fe/H] ranging from –1.80 to –1.30 dex, and also found that the cluster hostsat least two distinct populations separated in [Fe/H] by ~0.25 dex.

2.2 Instrumentation

I used high-precision photometric images taken from the archive of two different instruments on board the Hubble Space Telescope:
✓ The Advanced Camera for Surveys (ACS) is a so-called third generation Hubble instrument, with a wide field of view, high image quality and sensitivity, and its

wavelength range extends from the ultraviolet out to the near infrared. It can also perform spectroscopy through a grism. ACS is made up of three sub-instruments:

✓ Wide Field Channel (WFC), a high efficiency, wide field optical and near-infrared camera. It is optimized to hunt for galaxies and galaxy clusters in the remote and ancient Universe.
Wavelength range WFC: 350-1050 nm

✓ High Resolution Channel (HRC), a camera designed to take extremely detailed pictures of the light from the centres of galaxies, star clusters and gaseous nebulae where planetary systems may be hidden.
Wavelength range HRC: 200-1050 nm

✓ Solar Blind Channel (SBC) blocks visible light to allow faint ultraviolet radiation to be discerned. It can be used to study weather patterns on other planets and aurorae on Jupiter.
Wavelength range SBC: 115-180 nm

✓ The Wide Field Camera 3 (WFC3) offers comparable performance to the ACS but over a wider range of wavelengths, and with respect to its predecessor WFPC2 has an improved resolution over a wider field of view. This instrument has two independent channels, one for ultraviolet and visible light (UVIS) and the other for near infrared (NIR). In detail:

✓ UVIS channel
Spectral range: 200-1000 nm
Detector type: silicon-based CCD
Detector array size: 4096x4096 px
Field of view: 160x160 arcsec

✓ IR channel
Spectral range: 850-1700 nm
Detector type: mercuric cadmium telluride (HgCdTe) array
Detector array size: 1024x1024 px
Field of view: 123x137 arcsec

The relative filters that I used were F336W, F438W (both WFC3/UVIS), F55W, F814W (both ACS/WFC).

2.3 Dataset

I started from 28 raw images downloaded from the HST archive, subdivided in the four mentioned filters: 6 images for F438W and F814W and 8 for F336W and F555W. These were calibrated, flat-fielded exposures corrected for the effects of the poor charge transfer efficiency (CTE) of the detectors (_flc, Anderson & Bedin 2010). I repeated for each filter the same procedure, described in next paragraph.

The following are the characteristics of the images, common to all:
- ✓ Date of observation: 13/06/2016
- ✓ Right ascension: $17^h\,02^m\,38.7^s$
- ✓ Declination: -26° 16' 11.6''
- ✓ Delta RA: 0.22^s
- ✓ Delta Dec: -0.11''

We can notice that the instrumental values of right ascension and declination are almost equal to those taken from the astronomical database of SIMBAD reported in paragraph 2.1, differing only in few seconds.

Table 2.1 lists the main properties of each image constituting my dataset.

2.4 Point spread function

In the process of reduction of astronomical images, the analysis of the point spread function is fundamental. The PSF is the response of the instrumental system to the illumination by a point source as the stars are. The nature of this function is changeable and not fixed as it would be in an ideal situation, since it varies between different exposures owing to little variations of the focus, of the mechanical parts of the detector, and to residual charge transfer efficiency.

On its focal plane, the telescope produces an instrumental PSF (iPSF), which is a function that gives the flux of a point source as a function of offset from its centre. But what astronomers are interested in is the *effective point spread function* (ePSF), a continuous function defined as the convolution of the instrumental PSF and the function of the spatial sensitivity of each pixel. A significant property of this ePSF is that the expectation of any pixel in any image of a star is the product of the ePSF

Image name	Instrument	Filter	Exposure time (s)
iczd01sgq	WFC3/UVIS	F336W	685
iczd01s3q	WFC3/UVIS	F336W	674
iczd01rqq	WFC3/UVIS	F336W	659
iczd01rdq	WFC3/UVIS	F336W	566
iczd01rsq	WFC3/UVIS	F336W	350
iczd01rfq	WFC3/UVIS	F336W	350
iczd01s5q	WFC3/UVIS	F336W	350
iczd01siq	WFC3/UVIS	F336W	350
iczd01rhq	WFC3/UVIS	F438W	350
iczd01ruq	WFC3/UVIS	F438W	350
iczd01s7q	WFC3/UVIS	F438W	350
iczd01skq	WFC3/UVIS	F438W	350
iczd01s0q	WFC3/UVIS	F438W	10
iczd01rcq	WFC3/UVIS	F438W	10
iczd01rjq	ACS/WFC	F555W	350
iczd01rwq	ACS/WFC	F555W	350
iczd01s9q	ACS/WFC	F555W	350
iczd01smq	ACS/WFC	F555W	350
iczd01rnq	ACS/WFC	F555W	10
iczd01rpq	ACS/WFC	F555W	10
iczd01sdq	ACS/WFC	F555W	10
iczd01sfq	ACS/WFC	F555W	10
iczd01rlq	ACS/WFC	F814W	348
iczd01ryq	ACS/WFC	F814W	348
iczd01sbq	ACS/WFC	F814W	348
iczd01soq	ACS/WFC	F814W	348
iczd01sqq	ACS/WFC	F814W	10
iczd01s2q	ACS/WFC	F814W	10

Table 2.1 Summary of some singular properties of the images used in this work, besides the global properties listed above.

value in the centre of a given pixel with respect to the centre of the star and a factor that depends on the luminosity of that star.

In the images taken from HST, stars of globular clusters appear to be point sources and relatively isolated, so in this case we need three parameters to get a complete description of each of these objects: the two coordinates of position x, y and the total flux f. We can derive these values performing a fit of the point spread function to the array of pixels constituting the image of the star.

To gain an adequate degree of accuracy, we need an iterative procedure to construct our PSF models, as we will see in next paragraph.

2.5 Methods

First-pass photometry

Starting from the 6 or 8 measurements of magnitude *m* and positions *x*, *y*, I wanted to mediate them to obtain a single value for each of the three quantities.
The models of PSF were obtained using a series of fortran routines developed by Jay Anderson (2000). The first was *img2psf*, which works iteratively on bright, isolated and non-saturated stars, inside a certain number of cells specified by one of the arguments. The program starts from the archive PSF fitting the stars in each cell, and using the residuals of the fit develops at each iteration an improved PSF model basing on 7 input arguments:
-   HMIN, minimum distance between sources, in pixels (used 13);
-   FMIN, minimum flux of a star in order to be examined, in counts (used 5000);
-   PMAX, maximum flux, in counts. There is a limit for saturated stars, which for HST is at a value of 55000 (used 54600);
-   QMAX, maximum q_{fit}, that is the parameter describing the quality of the fit ($0<q_{fit}<1$, used 0.3);
-   NSIDEs, number of cells in which dividing the image in order to sample the PSFs (between 1 and 5, used 2);
-   PSFFILE, selection of the archive PSF for the first iteration;
-   IMG, selection of the images to analyze.
The results of this elaboration were *fits* images made of a 7x8 grid of PSFs for each image selected in the IMG argument (figure 2.1).

Figure 2.1 One of the resulting 7x8 grids of PSFs.

Next step was to use another fortran routine, *img2xym*, to determine magnitudes and positions of stars employing the newly produced best-model PSFs fitting them to the stars of our images. The required arguments were 5:
- HMIN (used 5);
- FMAX (used 100);
- PMAX, this time without considering the saturation limit (used 999999999);
- PSFFILE, using the just created PSF models, one by one;
- IMG, this time each image one by one.

The results of this elaboration were files containing the list of *x* and *y* coordinates, magnitudes and the q_{fit} parameter of the sources extracted from each image. The latter allows to discriminate between real stars and other sources. Ideally a $q_{fit} \sim 0$ would mean a perfect fit between the measured star and the best-model PSF, but practically it is a measure of a saturated source, while the brightest stars have a small value.

The position coordinates were given in the reference frame of the images, thus in order to obtain the mean coordinates and magnitudes I needed to bring these quantities in a common reference frame through a transformation, and this was done later on.

At this point, having these parameters describing the sources identified in our images, I wanted to remove the "bad" stars, namely the non-stellar sources, as cosmic rays, noisy or dark current pixels and so on. This was done employing a macro in *Supermongo* which task is to clean our files basing on the q_{fit} parameter. This macro develops a plot of the q_{fit} as a function of the magnitude in the filter we are using, selecting only the best measurements which lie under a line that is the linear interpolation of a computation based on the median q_{fit} (figure 2.2). In detail, this program divides the x axis of magnitudes into a certain number of bins depending on the number of stars, then for each of them the median q_{fit} (red points in figure) is computed recursively and all stars exceeding $2 \times 2\sigma$, with σ standard deviation, are momentarily excluded until with the successive iteration the median is computed again. All these steps are repeated until the difference among two successive measures of the median results smaller than 1%. Then, adding to the median of each bin N times σ (with the factor N=4 in my case), the final task of the program is to linearly interpolate these median points, obtaining the blue line shown in figure, which separates the well-measured sources (black points) from the sources that are poorly fitted by the PSF model (blue points).

The result of this elaboration was a catalog for each image containing the two coordinates of position and the magnitude of the selected stars.

As previously said, the positions *x*, *y* needed to be corrected for the effect of distorsion since each measurement has been carried out in its own reference frame, so it was necessary to transform them to a common one.

For this purpose I employed the fortran routine *xym2mat*, which works in two steps. To begin, for each filter a photometric zero point had to be chosen, for which I took the image with the deepest exposure as the common reference frame to construct the photometric master frame. Then the program starts after requiring one argument consisting of the distance in pixels from a given star within which the program can search for common stars (used 15). It finds the same stars in different catalogs by means of a method named *cross identification* which uses the bright and unsaturated stars well fitted by the PSF (for which I put a limit on magnitudes of $m > -13.6$) searching for similar triangles of stars among the current frame and the master one. The coordinates derived in this way are used to calculate the linear transformation composed of six parameters that are the three coefficients of each of the two linear equations in two unknown *x* and *y* describing the position of the same star in the master frame and in the reference frame of the considered image from time to time.
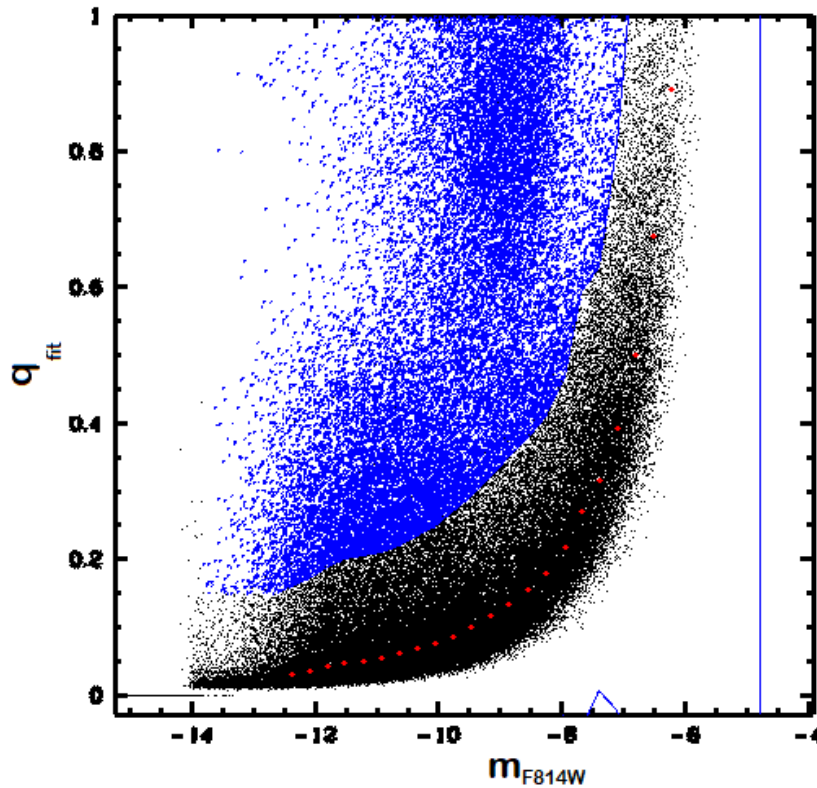
Figure 2.2 Elaboration of the *Supermongo* macro "clean". Black dots are the maintained stars while blue dots are the rejected sources. The red, bigger dots represent the median q_{fit} value for every bin of magnitude.

This transformation was used to calculate the difference between the magnitudes in the master frame and in each exposure, then the mean of these magnitude differences allowed to convert the coordinates of the stars in the various images into this common reference frame, the master frame.

The result of this elaboration was a file for each image, named MAT.00x (with x going from 1 to 6 or 8 depending on the number of images in the filters), including position and magnitudes in both the starting reference frame and the master frame, and the residuals of the transformations.

Then I performed a check of the accuracy of this elaboration analyzing the residuals, which ought to have a spherical distribution around the 0.

These MAT files were necessary for the next program to be used, *xym2bar*, which calculates the mean positions and magnitudes of stars with $m < -5.0$, giving as a

result one catalog for each filter. It required one single argument consisting of the minimum number of different frames in which the same star needed to be identified in order to be taken into consideration (used 2).

The last fortran routine to be used was *xym1mat*, which, given two catalogs of different filters, finds the same stars in the different catalogs, organizing them in the same order producing another catalog with ordered positions and magnitudes. This work was done for each of my four filters using as reference filter the F814W, thus obtaining at the end a catalog for every filter linked to the F814W.

At this point we have to take into account that the reference frame of the Hubble Space Telescope, to which the four filters F336W, F438W, F555W, F814W pertain, is arbitrary, since its axes are not linked in any way to the celestial coordinates. We want, on the contrary, to align our coordinates *x*, *y* to the coordinates of right ascension and declination, respectively, and for this purpose I employed the GAIA catalog, which I downloaded from the archive (GAIA Data Release 3). Indeed this catalog contains stars having position coordinates oriented along the celestial coordinates, but I had to initially transform them from spherical (right ascension, declination) to linear (*x*, *y*), and this was done employing the command *rd2xy* in Supermongo. Then I used one more time the *xym1mat* program, through which I could find the geometrical transformation to pass from the arbitrary HST frame to the absolute frame of GAIA. In this case the program identifies the stars included in both catalogs by means of the same method of cross identification described for *xym2mat*. Then the couples of coordinates found in the different catalogs corresponding to the same star are used to derive the linear transformation with six parameters which allows to switch from one frame to the other. Employing this procedure for all four filters I obtained a new catalog for each one with the stars oriented in the universal reference frame.

Second-pass photometry

Now that we had all catalogs brought to the same reference frame, we wanted to make them as complete as possible in terms of identification of stars in the field. This was done using the fortran program *kitchen_synk2* (KS2, Anderson et al. 2008). The starting material on which KS2 works are the exposures of each filter, the MAT files previously produced that contain the transformation between images and the master frame, and the perturbed PSFs. This software is able to handle more filters and more images simultaneously, and to find and measure faint stars. To do this, KS2 performs several iterations, first identifying the brightest and most isolated

stars, computing their fluxes and positions and subtracting them from the image. It also generates a mask for these bright stars, including saturated sources, in order to exclude factitious sources and also to improve the detection of faint stars near to bright ones. Then, in the successive iterations it finds, measures and subtracts stars that are progressively fainter. In each exposure stellar fluxes and positions are measured separately, then are averaged together to derive their best determinations.

The KS2 software employs three methods to detect and measure stars, basing on different ranges of their luminosity.

✓ Method 1

It is applied to bright stars, which produce a peak well distinguishable inside the area of 5×5 pixel within the center of the star. Using the local PSF the program measures the flux and the position of each star, then the final values for a filter are computed as the mean of fluxes and positions in the single images, while the level of the sky is estimated in the annulus between 4 and 8 pixels from the centre of the considered star.

✓ Method 2

It is applied to faint stars, specifically those which do not generate a significant peak in the exposures, therefore the previous method would not be suitable to detect them. In this case the program subtracts the neighbour stars, then executes the aperture photometry of the star in the 5×5 pixel raster, weighting each pixel in order to assign low weight to pixels that are contaminated by nearby stars. The sky is calculated as in method 1.

✓ Method 3

It is applied to faint stars in crowded regions. It follows the same mode of operation of method 2 but aperture photometry is computed on pixels inside a radius of 0.75 pixels from the centre of the star. The level of the sky is estimated in the annulus between 2 and 4 pixels from the position measured during the finding stage.

In figure 2.3 (Milone et al. 2022) there is a comparison of the colour-magnitude diagrams of the star cluster Lindsay 1 computed with the three different methods. From the top panels one can see that methods 2 and 3 are optimal for faint stars since they provide well-defined main sequences. The first method, instead, produces the best photometry for stars with bright instrumental magnitudes as shown by the narrow RGB and SGB sequences in the bottom left panel.

For my final catalog I took the data derived from the first and the second method. The catalog thus obtained contained for each star the spatial coordinates, the

magnitudes in each filter, the root mean square and the NF value (which is the number of images in which a specific star has been measured). To achieve the conclusive catalog of the procedure of data reduction, I finally needed to correct the magnitudes for differential reddening.

2.6 Photometric calibration

The final step of data reduction was photometric calibration that consents to give a physical meaning to the instrumental magnitudes we used in the previous passages.
This process was based on the comparison between instrumental magnitudes, measured by the _flc images employed so far, and magnitudes of aperture photometry, measured by another type of image which are the _drc.
Photometry of the filters employed in my analysis has been calibrated to the Vega magnitude system by computing the aperture correction to the magnitudes derived with the PSF photometry and applying to the corrected instrumental magnitudes a photometric zero-point. The aperture magnitudes were measured within circular regions of 0.4 arcsec for UVIS/WFC3 and 0.5 arcsec for WFC/ACS, using _drc images which are drizzled and corrected for charge transfer efficiency. The peculiarity of this type of images is that they have exposure time normalized to 1 second so that the pixel values coincide with the number of photons counts per second. Then calibrated magnitudes were derived summing the following quantities:

$$m_{cal} = m_{inst} + \Delta m + m_{ap} + zp_{filter}$$

where besides the instrumental magnitude (m_{inst}) there is the contribution of the computed 3σ-trimmed mean of the difference between PSF photometry magnitudes and aperture photometry magnitudes (Δm), the aperture photometry correction (m_{ap}) and the zero-point correction for a specific filter (zp_{filter}).
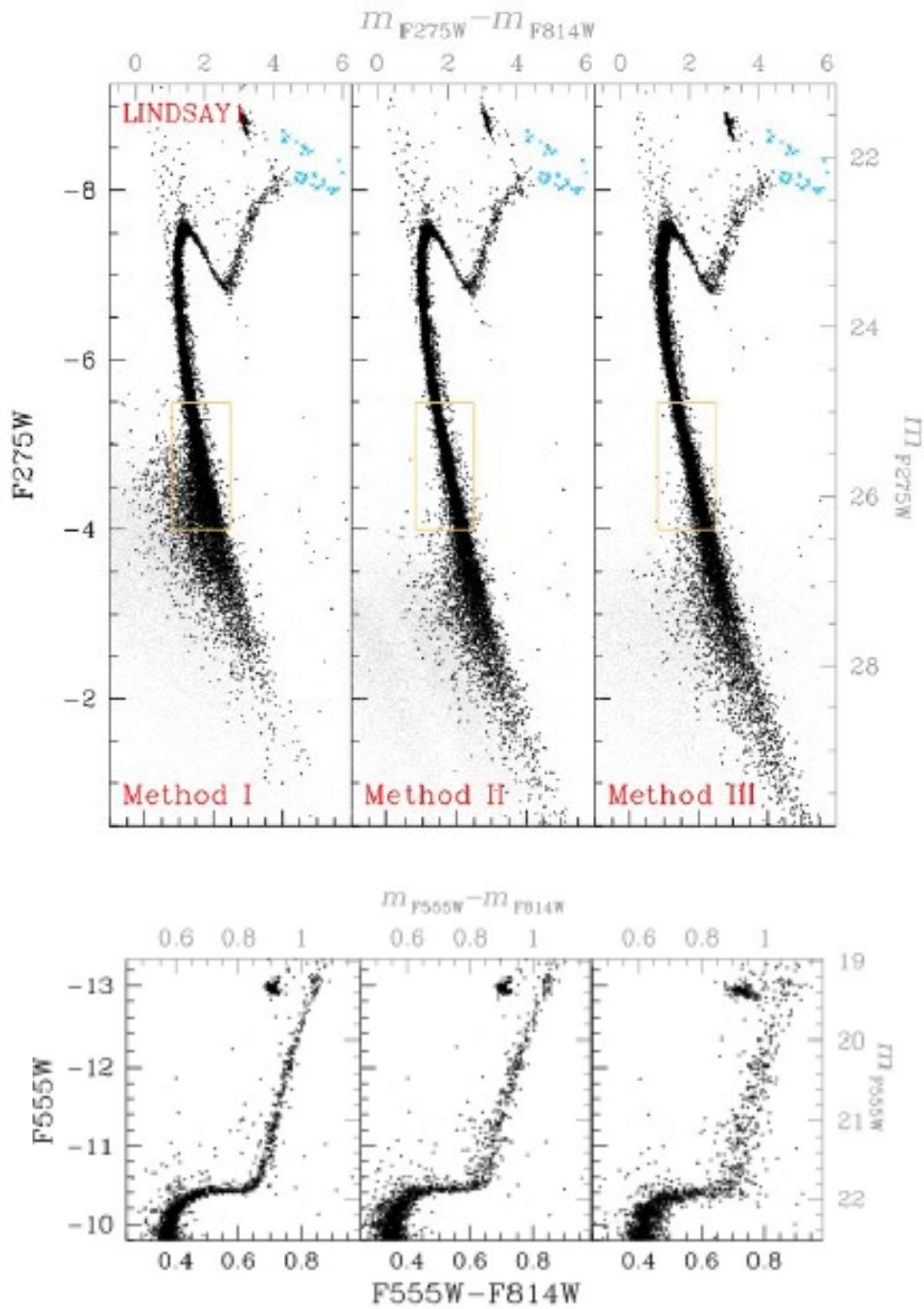
Figure 2.3 On top, m_{F275W} vs. $m_{F275W} - m_{F814W}$ CMDs of the cluster Lindsay 1 computed with the three methods of KS2. In black are well-measured stars, in light gray are stars with poor photometry, in light blue are stars where the F814W magnitude is derived from saturated images. On bottom, the region of m_{F555W} vs. $m_{F555W} - m_{F814W}$ CMDs populated by bright stars with $m_{F555W} < -9.75$ (Milone et al. 2022).

2.7 Correction for differential reddening

NGC 6273, as all celestial objects outside the Solar System, is affected by differential reddening, which alters the values of magnitude compromising the entire data analysis. While this effect and its origin are described in next chapter, in this section I focus on the procedure that was employed to correct it (Milone et al. 2012):

✓ It starts establishing the direction of the line of reddening, given by the following formula:

$$\vartheta = arctg \frac{A_X}{A_X - A_{F814W}}$$

with A_X being the absorption coefficient in the different bands X=F336W, F438W, F555W, F814W, and A_{F814W} in the F814W.

✓ The aim is to construct a photometric reference frame whose axes of abscissa and ordinate are respectively parallel and orthogonal to the reddening direction. The origin of this frame corresponds to a reference star selected in the CMD region where the reddening direction draws a wide angle with the cluster fiducial line so that one can disentangle the effect on stellar colours and magnitudes due to differential reddening from the shift due to photometric errors. Indeed the former is responsible for a systematic shift of stars along the reddening line, while the latter is responsible for a random scatter along the fiducial line.

✓ To get to this new reference frame for the CMDs, a translation and a counterclockwise rotation by an angle ϑ are performed.

✓ For stars of main sequence, subgiant branch and redgiant branch, fiducial lines are produced. Initially a sample of stars along these sequences is selected and divided into ordinate bins. For each bin, the median abscissa associated with the median ordinate of the star in that bin is computed, and the fiducial line is derived by the linear interpolation of these median points.

✓ The distance of the reference star from the fiducial line is computed along the reddening direction, then also its projection along the colour direction. These latter values, $\Delta(m_X - m_{F814W})$, which are the observed ones, are compared with analogous quantities derived from the isochrones and corresponding to reddening variations going from $\Delta E(B-V) = -0.3$ to 0.3 following steps of 0.001. Performing the test of χ^2, the value of $\Delta E(B-V)$ that produces the minimum result is assumed as the best estimate of differential reddening associated with the reference star considered.

- ✓ To get the amount of differential reddening associated with each star of the catalog, I took a sample of N reference stars, and the best determination was provided by the median of the $\Delta E(B\text{–}V)$ values of these N stars.
- ✓ In addition, the value of N was varied (ranging from 35 to 150 in steps of 5 or 10) obtaining different determinations of $\Delta E(B\text{–}V)$ for each of which was computed the colour distance between the corrected abscissa value of the reference star and the fiducial line. The best determination of differential reddening was given by the value of N that produced the minimum root mean square of these distances.

The magnitudes corrected in this way were finally included in the catalog.

In figure 2.4 there is an example of colour-magnitude diagram representing the m_{F336W} vs. $m_{F336W}\text{–}m_{F814W}$, before and after being differentially dereddened. It is evident the change in the broadening of the stellar sequences, with the corrected diagram that gets significantly narrower along both axes.
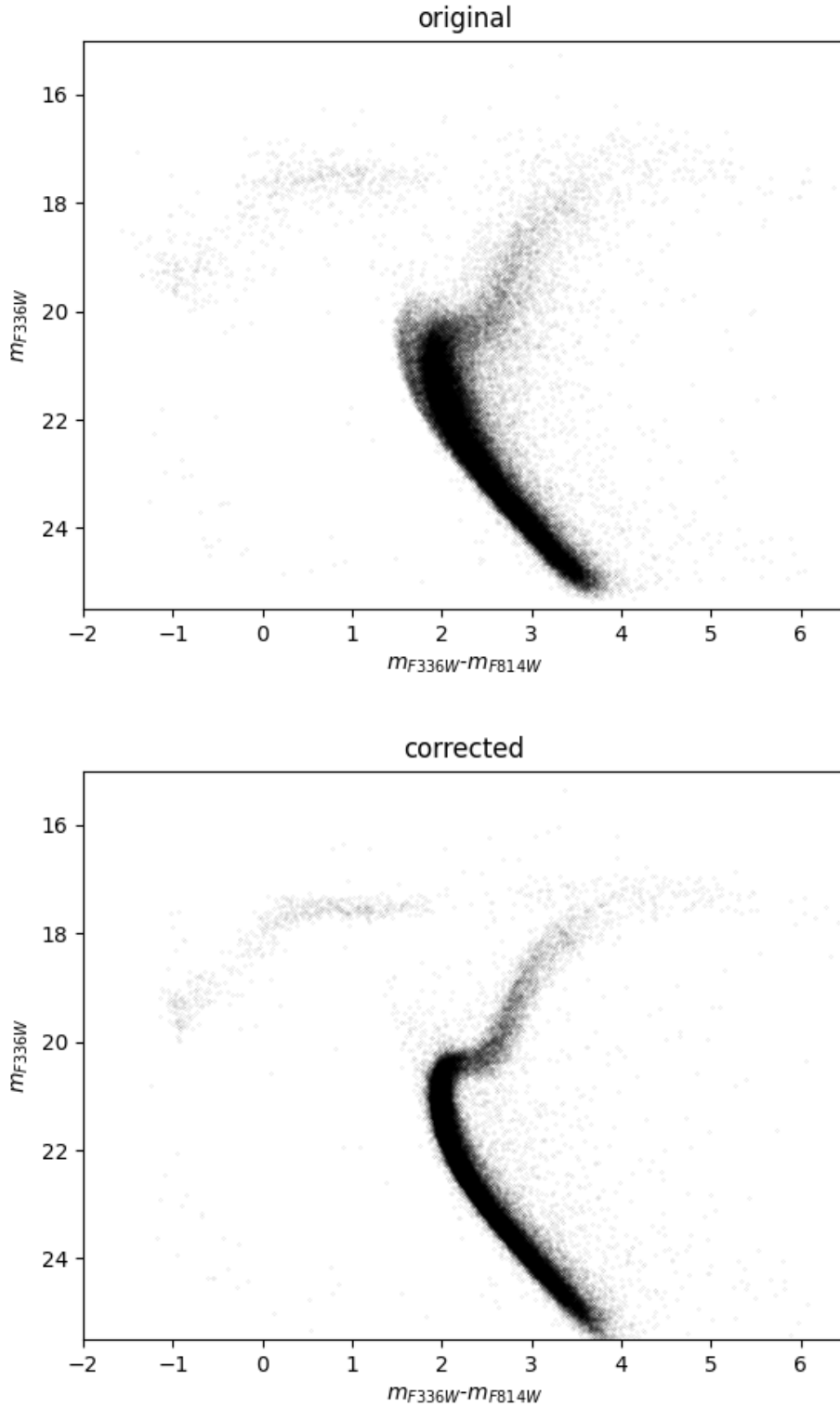
Figure 2.4 Comparison of the m_{F336W}–m_{F814W} vs. m_{F336W} CMD as observed and its counterpart corrected for differential reddening. It is clearly visible the broadening on both axes of the not corrected panel on top with respect to the panel on bottom.

3. Data analysis and results

3.1 Differential reddening

Spatially-variable extinction or differential reddening occurs in all directions throughout the Milky Way but is most significant towards the Galactic centre, in low-latitude fields as is the case of our globular cluster NGC 6273.

This phenomenon is due to the fact that the interstellar medium permeating the interstellar space is composed by gas and dust which tend to scatter the radiation, so to absorb it and emit in different directions. Thus the incoming radiation loses energy and as a consequence the wavelength widens and objects appear redder than they really are ("reddening"). In addition this phenomenon is not uniform along the spectrum ("differential").

Introducing non systematic shifts in the actual colour and magnitude of the member stars located in different parts of a GC, differential reddening leads to a broadening of the evolutionary sequences in the colour-magnitude diagram. Thus it hampers the detection of multiple population sequences and the precise determination of some parameters as age, metallicity and distance of globular clusters.

As concerns the examined cluster NGC 6273, the significant amount of differential reddening is confirmed in a work already present in literature, the paper of Alonso-Garcìa et al. (2012) who have drawn an extinction map for the cluster field (figure 3.2), finding that the changes in the extinction across the field are significant ($\Delta E(B–V) \sim 0.3$) with the extinction that is higher towards the east and peaks in a small region located very close to the centre of the cluster. The area studied for this cluster in their work concerned a field of view of the inner 8.26 arcminutes of the cluster, basing on photometry from Earth. Complementary to this map was also the construction of the CMD (in $B–V$ and $V–I$ bands, figure 3.1) before and after the dereddening process, where in the second case the definition of the different branches is highly improved: the different sequences get tighter by almost a factor of two after being differentially dereddened, the presence of an extended blue HB is clearly visible and the location of the RGB bump is more easily identifiable.
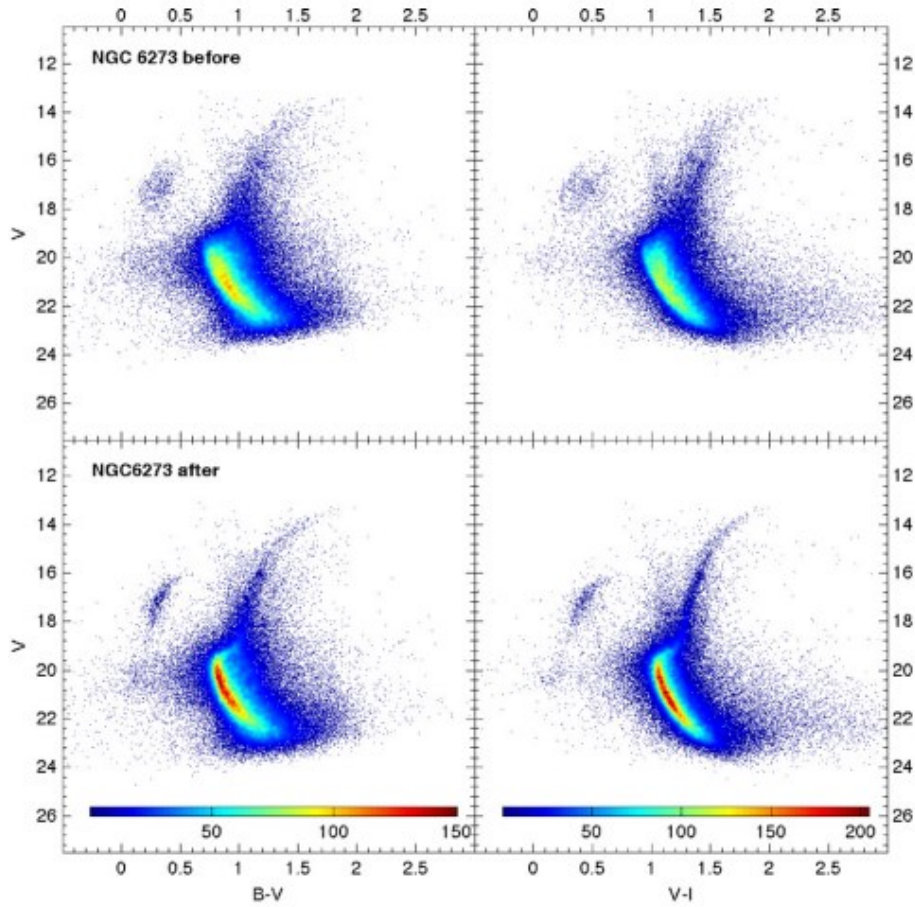
Figure 3.1 CMD of the cluster NGC 6273 before and after being differentially dereddened. Colour bars show the range in densities of stars in the CMD (×10⁴ stars per square magnitude, Alonso-Garcìa et al. 2012).
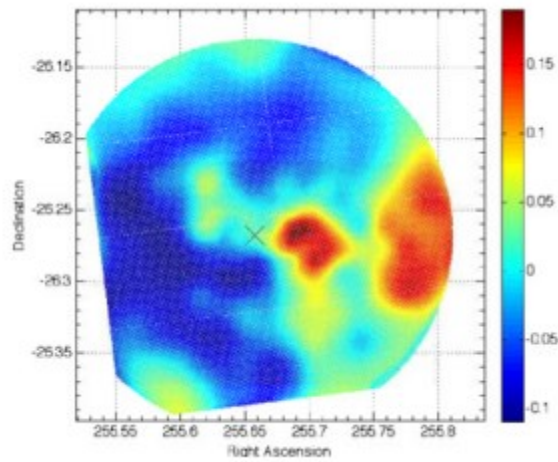

Figure 3.2 Extinction map for the cluster field. The × marks the position of the cluster centre, and the colour code gives the colour excess *E(B–V)* (Alonso-Garcìa et al. 2012).

A brief and qualitative comparison can be done between the results of Alonso-Garcìa et al. and those of this work, considering first of all that the conditions in which the data were collected in the two cases are significantly different. Indeed the former worked on the ground-based 6.5 Magellan Baade Telescope of Las Campanas Observatory, whereas I took the data from the space-based HST, entailing a difference on the quality of the images since the ground-based observations are affected by a series of atmospheric effects that introduce bias in measurements and affect the stability of the PSF, which, on the contrary, by space has a more stable trend.

In addition the two works differ also in the field of view used for the observations, with a FoV of 8.26×8.26 arcminutes against a size of 2.7×2.7 arcminutes in Alonso-Garcìa et al. and in this work, respectively. In a bigger region the variations in reddening are more present, thus impairing more importantly the measurements.

Keeping these differences in consideration, we can estimate the value of the differential reddening from my results. The calculation is performed as follows:

$$E(B - V) = \frac{A_{F814W}}{C} = \frac{m_{F814W}^{original} - m_{F814W}^{corrected}}{1.8557}$$

E being the colour excess, A the absorption in a particular band and C a tabulated constant. The differential reddening is then obtained from the difference between the maximum and the minimum values of the colour excess, resulting as:

$$\Delta E(B - V) = E_{max} - E_{min} = 0.246 - (-0.137) = 0.383$$

with the standard deviation as its error:

$$\sigma = 0.072$$

So despite our field of view was smaller than the one estimated by Alonso-Garcìa et al., thus less affected by variations of reddening, our $\Delta E = 0.38 \pm 0.07$ resulted slightly higher and this could be mainly due to the better resolution that HST has with respect to ground-based telescopes.

3.2 Colour-magnitude diagrams

The procedures discussed in chapter 2 and in section 3.1 provide us high-precision photometry corrected for differential reddening of the stars in the field of view of NGC 6273. The photometric bands that are available for NGC 6273 give us useful information for identifying and characterizing the multiple stellar populations.

In this context, the filters that I employed have the following characteristic features:

✓ F336W: comprises the wavelength range that includes the molecular band of NH. Hence, the flux of stars with similar luminosity in optical bands but different F336W magnitude provides us information on the nitrogen abundance of the distinct stellar populations (e. g. Marino et al. 2008, 2019).

✓ F438W: encloses the molecular bands of CN and CH. Hence it is sensitive to star-to-star carbon variations (e. g. Marino et al. 2008, 2019).

✓ The F555W, F814W filters are not significantly affected by molecular bands in RGB and MS stars. Nevertheless, the F555W–F814W colour is sensitive to the effective temperature of a star and can be an efficient tool to constrain stellar populations with different He abundances in monometallic GCs. Indeed, helium-rich stars are hotter than stars with canonical helium abundances and similar luminosity. Hence, they exhibit bluer F555W–F814W colours (e.g. D'Antona et al. 2005).

✓ In type II GCs, the F336W vs. F336W–F555W and the F336W vs. F336W–F814W CMDs are used to disentangle stars with different metallicities along the SGB, RGB and AGB. Specifically, metal-rich stars populate a faint SGB that is clearly connected with a red RGB sequence (e.g. Milone et al. 2018, Lagioia et al. 2019).

By combining colours and magnitudes in these four filters I obtained various colour-magnitude diagrams or pseudo-two-colour diagrams that highlight the main evolutionary phases of the stars in NGC 6273. In the following, I use the magnitudes corrected for the effects of the differential reddening:

$$m_X^{corrected} = m_X^{original} - A_X$$

Where X=F336W, F438W, F555W, F814W. The absorption coefficients are inferred from the reddening map by adopting the relations between $E(B–V)$ and A_x provided by Aaron Dotter (2016, private communication). As an example, I show in figure 3.3 the absorption in the F814W band as a function of the coordinates.
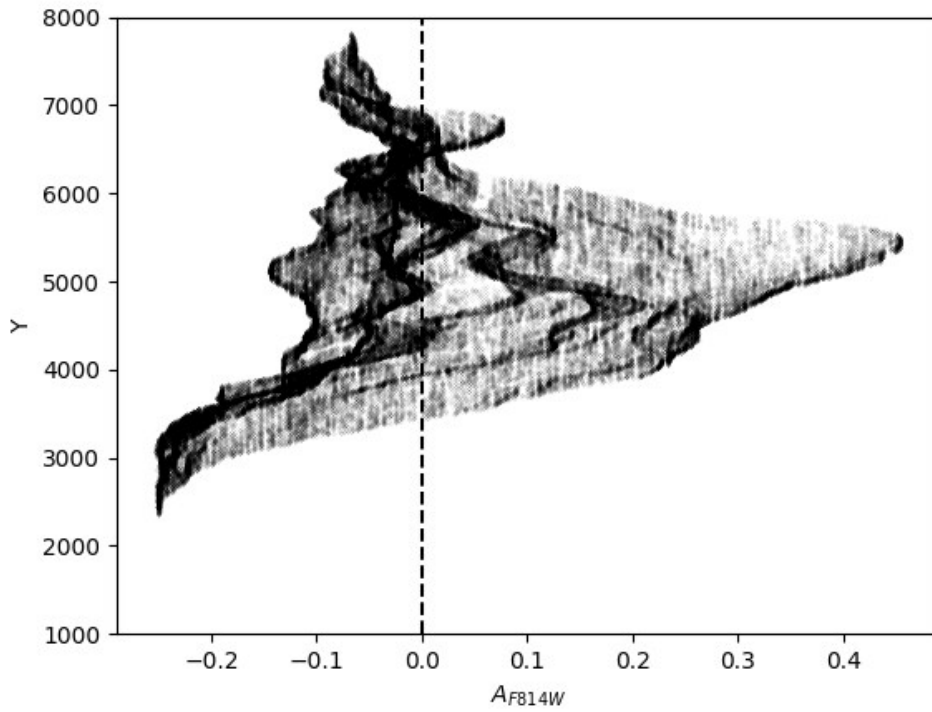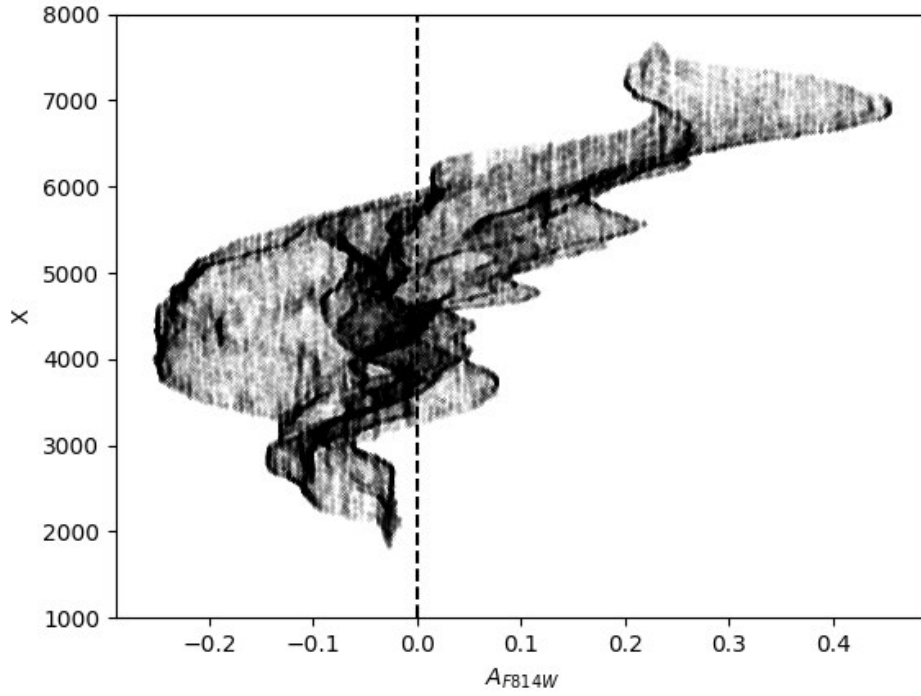
Figure 3.3 Absorption maps in the F814W filter against *x* (top) and *y* (bottom), in pixel units. The dashed line indicates the 0 value for absorption, that is $m_{F814W, observed} = m_{F814W, corrected}$.

Figure 3.4 shows the m_{F438W}–m_{F555W} vs. m_{F555W} CMD, which is similar to the classical B–V vs. V CMD but is constructed with the UVIS/WFC3 filters.

This CMD allows to identify the different evolutionary stages, which are highlighted by the coloured boxes and circles. Specifically:

✓ light green box encloses the majority of main sequence;
✓ rose box marks the MS region around the turn-off point;
✓ orange box includes most subgiant branch stars;
✓ red box refers to the red giant branch;
✓ red circle highlights the red giant branch bump
✓ green box encloses the asymptotic giant branch
✓ blue circle marks the blue stragglers
✓ light blue box refers to the blue horizontal branch
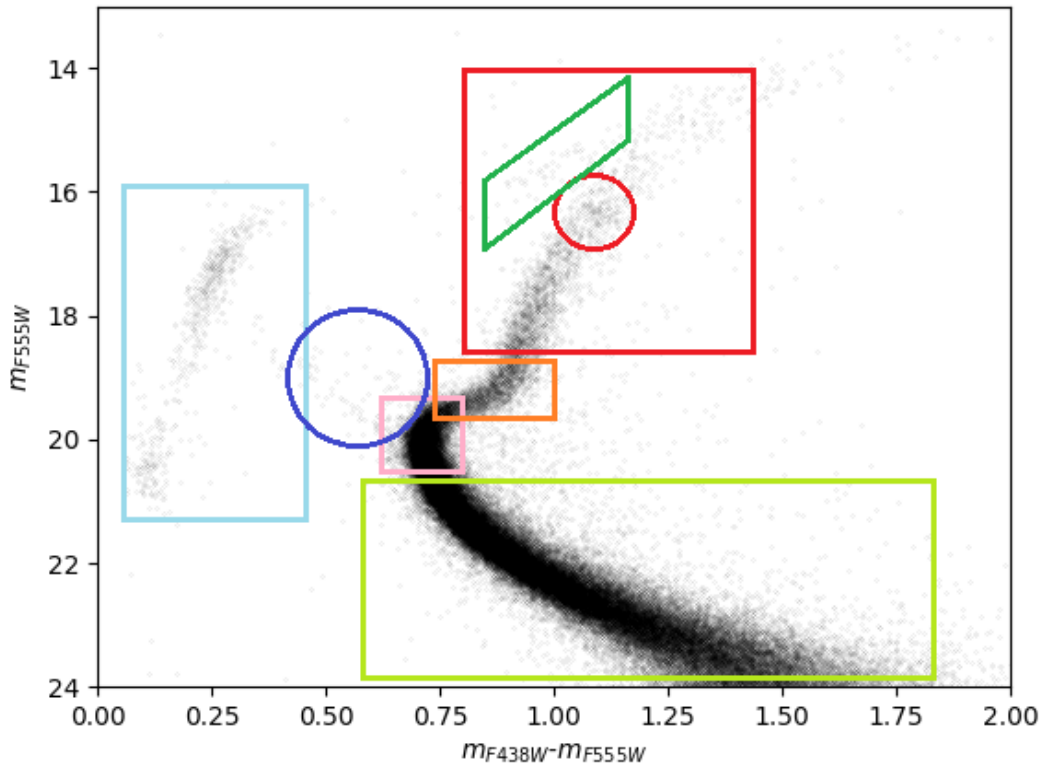
Figure 3.4 B–V vs. V CMD of NGC 6273 obtained from the corrected data. Boxes and circles frame the different stellar evolutionary phases (see text).

Similarly, the main evolutionary sequences of NGC 6273 are visible in the m_{F555W}–m_{F814W} vs. m_{F555W} CMD plotted in figure 3.5, analogous to the classical V–I vs. V CMD.

In the CMDs plotted in figures 3.4 and 3.5, which are constructed with optical filters it is not possible, however, to clearly disentangle the multiple populations of NGC 6273. On the contrary, the CMDs that involve the UV band, such as the m_{F336W}–m_{F438W} vs. m_{F336W} and m_{F336W}–m_{F555W} vs. m_{F336W} (figure 3.6) reveal that the SGB and the RGB of NGC 6273 are significantly much broad that the observational errors that for these bright stars are smaller than 0.02 mag in each colour, at the base of the RGBs.

Unfortunately, it is not possible to recognise multiple populations along the main sequence, possibly due to the larger observational errors of these fainter stars.
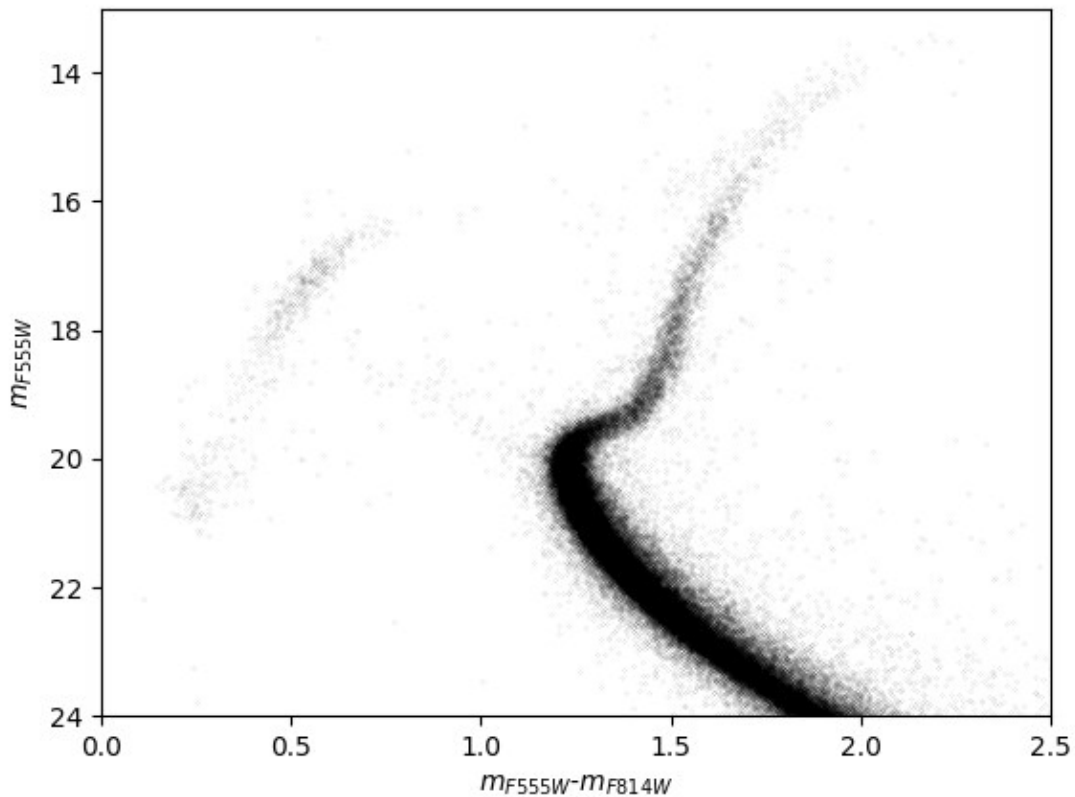
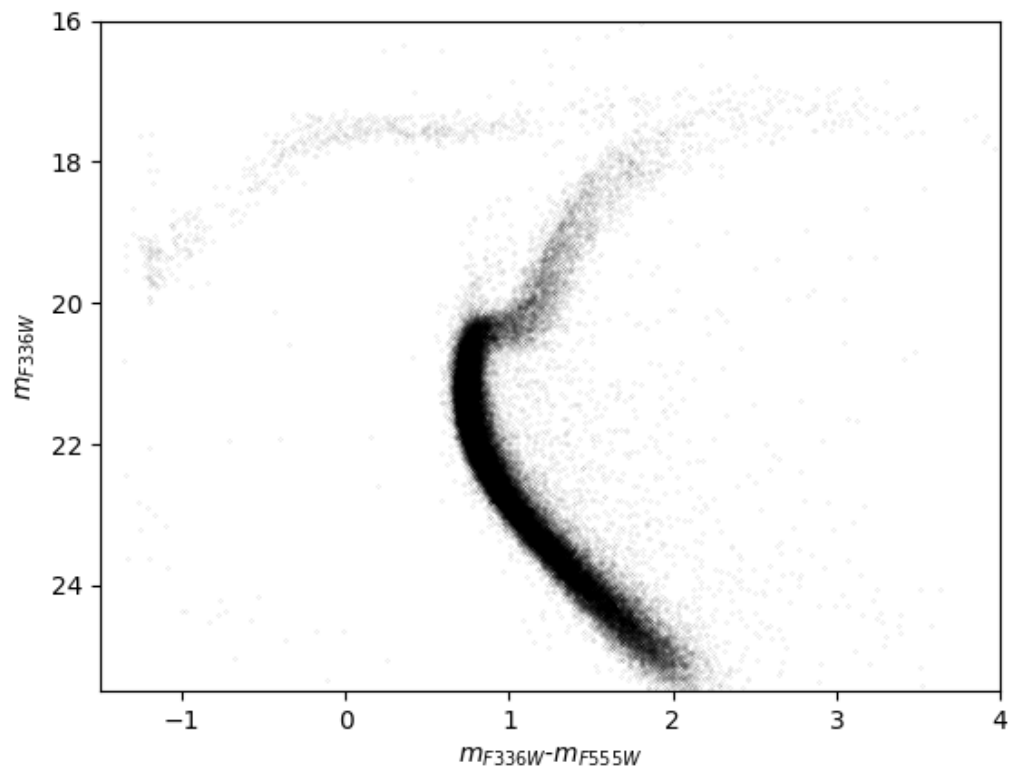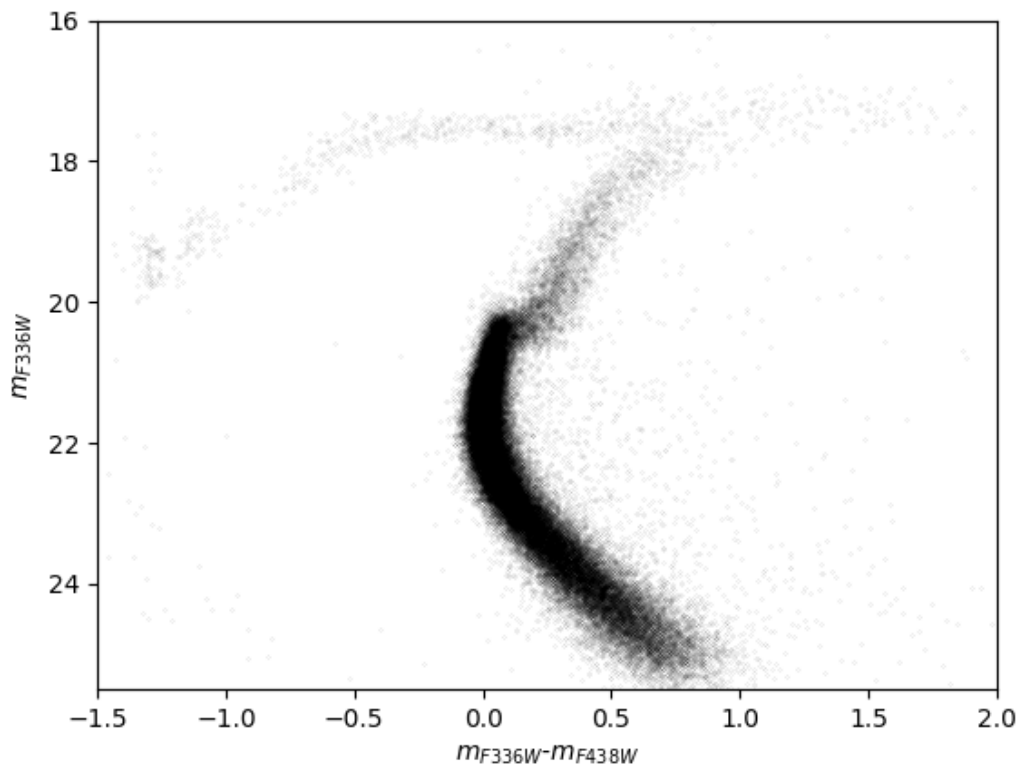Figure 3.5 *V–I* vs. *V* CMD of NGC 6273 obtained from the corrected data.

Figure 3.6 CMDs with optical-UV colours, where it is easier to separate stellar populations, particularly in the red giant branch where different sequences of points are visible.

Similar conclusions can be gathered from the pseudo-colour-magnitude diagram in figure 3.7 obtained by plotting the F814W magnitude against the colour difference:

$$C_{F438W,F555W,F814W} = (m_{F438W} - m_{F555W}) - (m_{F555W} - m_{F814W})$$

This diagram, which has been introduced by Marino et al. (2015) and is similar to the m_1 Stroemgren index, is sensitive to stellar populations with different metallicities. The fact that the RGB stars (black points in the figure) exhibit a wider range of pseudo-colour than that expected from the observational uncertainties alone (which are smaller than 0.03 mag for RGB stars) corroborates the evidence from papers based on spectroscopy (e. g. Johnson et al. 2015) that NGC 6723 hosts stellar populations with different iron content.

To better disentangle the stellar populations with different metallicities along the RGB, I constructed the photometric diagram chromosome map by using the m_{F814W} vs. m_{F336W}–m_{F438W} CMD and the m_{F814W} vs. $C_{F438W,F555W,F814W}$ pseudo-CMD (Milone et al. 2015, 2017, Cordoni et al. 2023). The ChM of a GC is a pseudo-two-colour diagram that maximizes the separation of multiple stellar populations with different chemical composition. The main difference between the ChM and the traditional two-colour diagram is that the colours plotted in the abscissa and the ordinate of the ChM are verticalized on both axes. I derived the ChM of RGB stars plotted in figure 3.8 by using the methods and the computer programs by Milone et al. (2017) and refer to their paper for further details on the methodology.

In the case of a monometallic stellar population, all stars would distribute nearly in a single blob around the origin of the reference frame, and their colour broadening would be entirely due to the observational errors. As emphasized in figure 3.9, the ChM of figure 3.8 reveals that NGC 6273 hosts two main stellar populations with different metallicities. The metal-rich stars, which are coloured red in figure 3.9, comprise the $40 \pm 2\%$ of the total number of RGB stars.
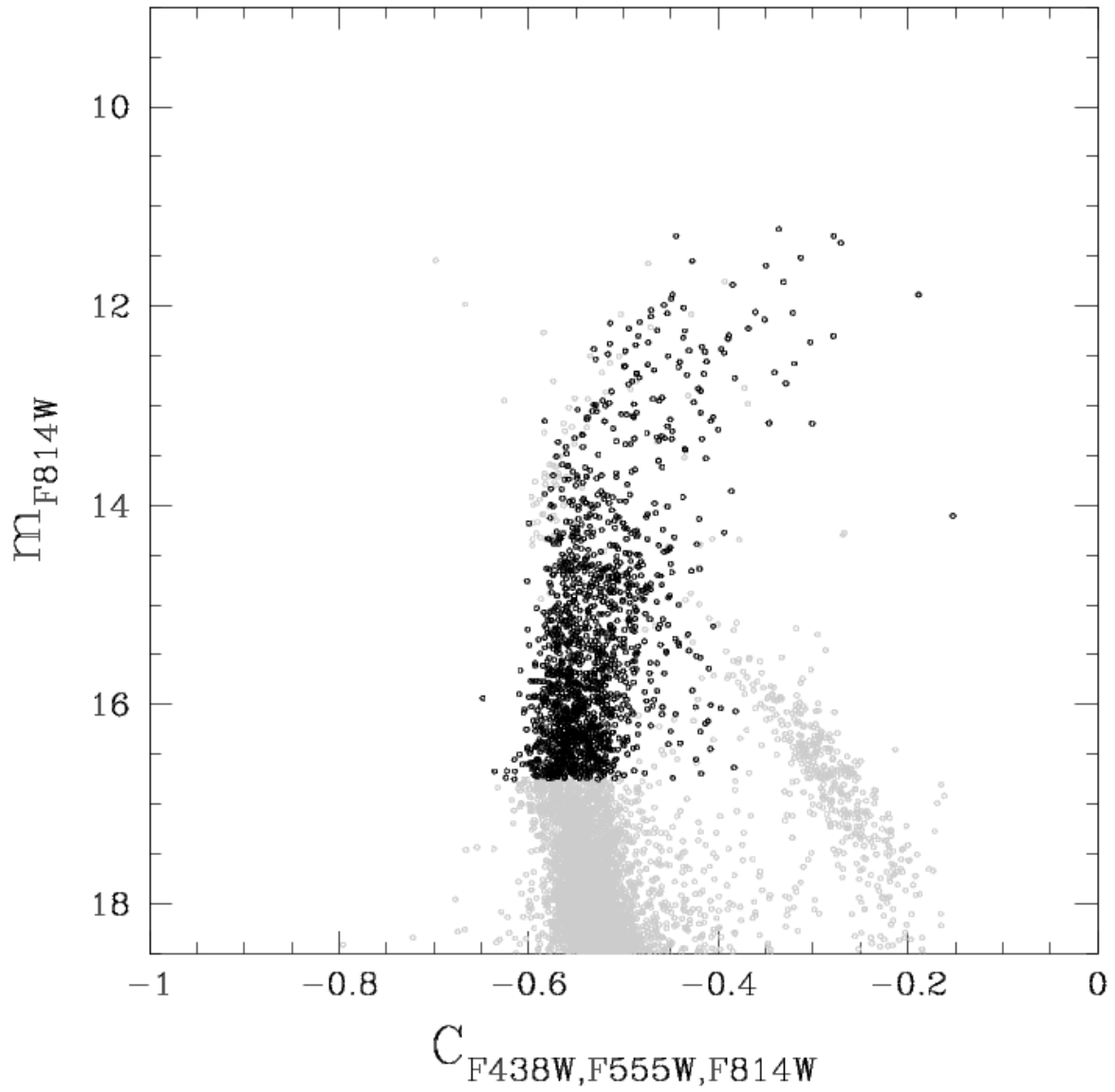
Figure 3.7 Pseudo-CMD m_{F814W} vs. $C_{F438W,F555W,F814W}$ where it is visible how the black dots, representing RGB stars, span a broader range of pseudo-colour than that expected from the observational uncertainties alone.
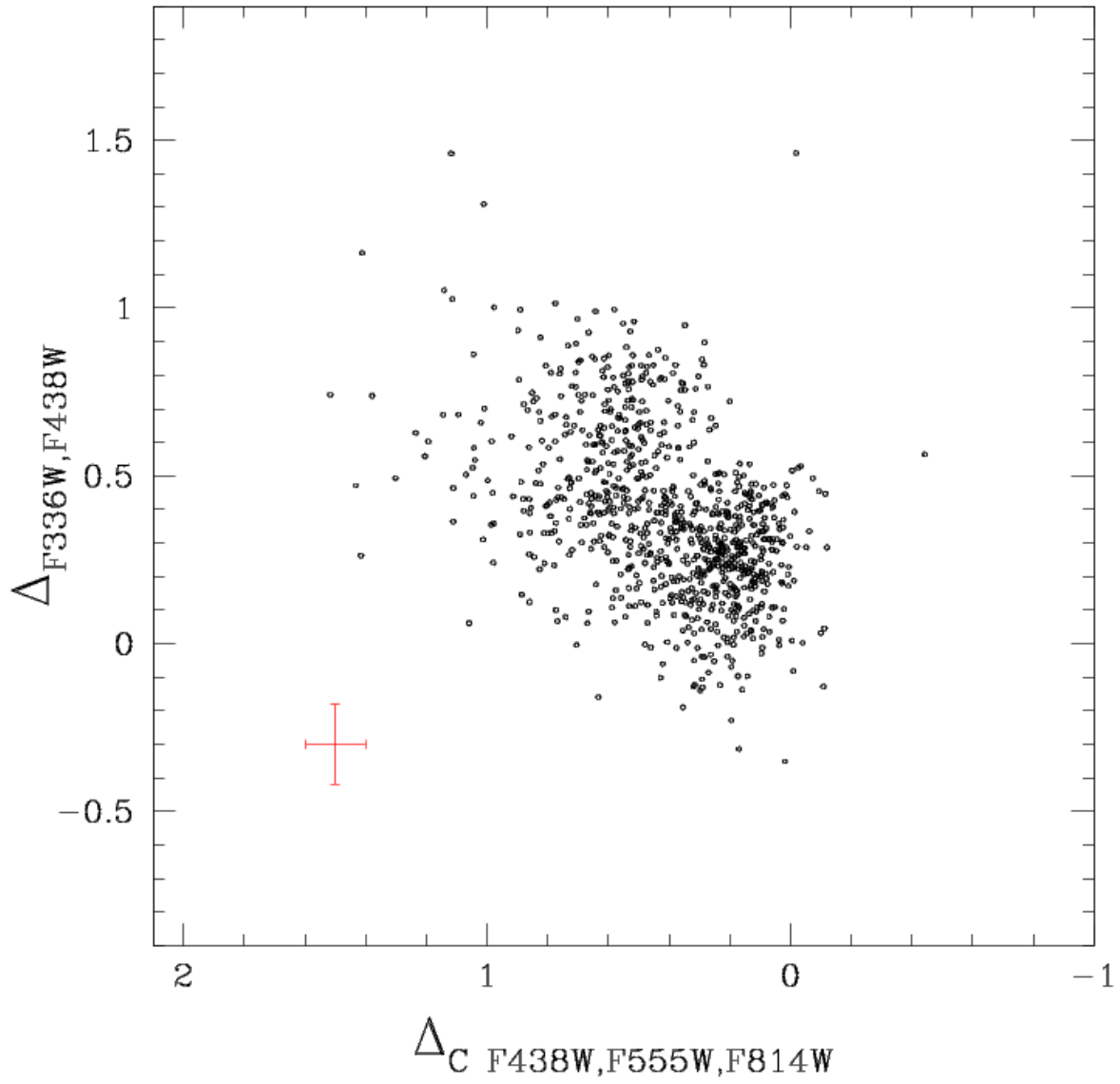
Figure 3.8 Chromosome map of NGC 6273, where we can glimpse two blobs representing two populations with different metallicity of the RGB stars considered in figure 3.7.
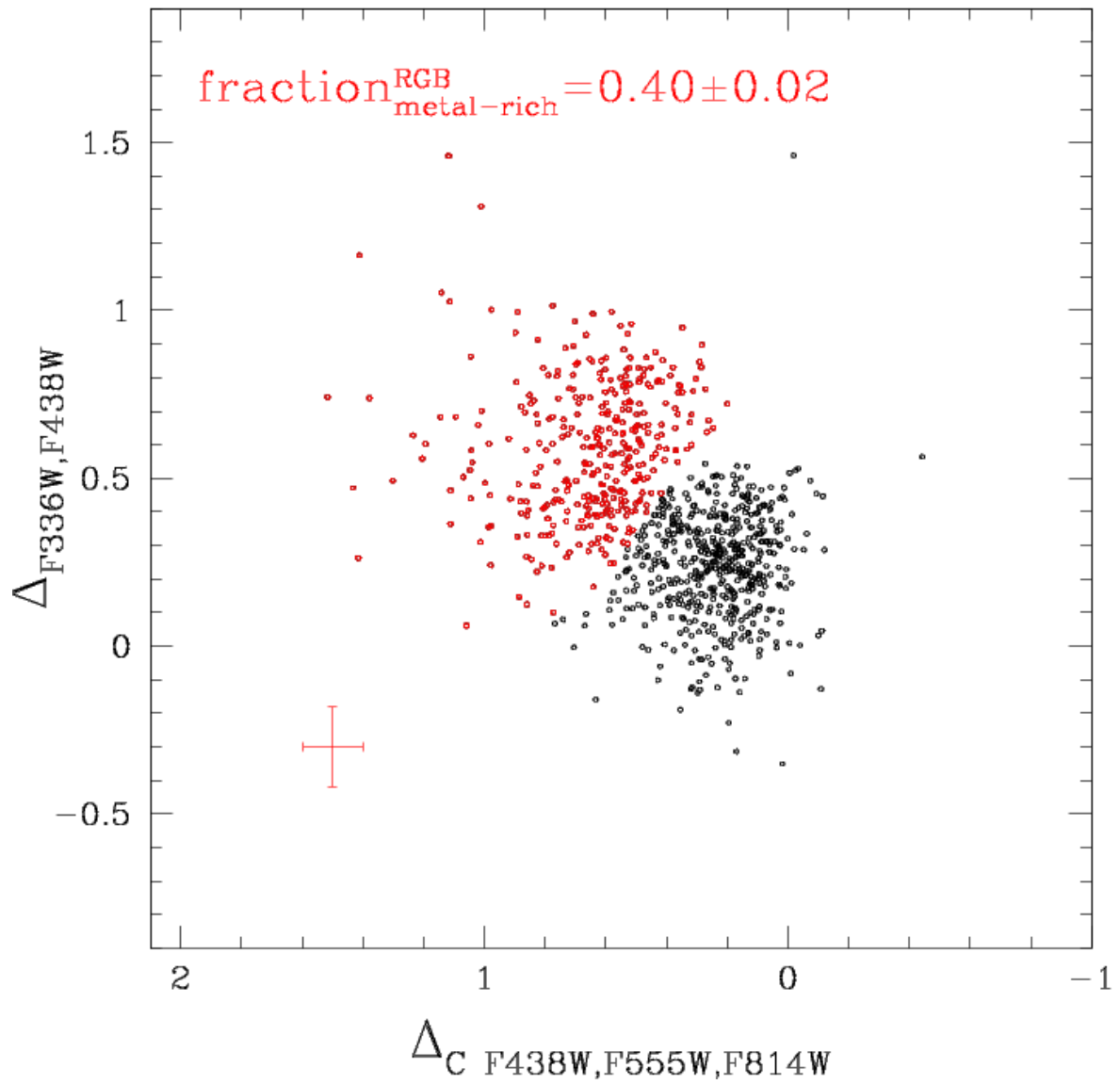
Figure 3.9 As in figure 3.8 but with the RGB metal-rich population highlighted in red, resulting to constitute the 40±2% of the total ensemble.

3.3 Measurement of RGB width

As already mentioned, the photometric footprint of the presence of multiple populations in GCs is given by the colour spread of the stars in CMDs constructed with specific magnitude and colour combinations sensitive to the content variation of light elements and helium, which is obtained with ultraviolet and optical bands. This spread results indeed to be larger than the photometric errors alone. The extension of the chemical spread in a given cluster can be quantified using a common metric, given by the colour extension or width of the red giant branch in CMDs.

In this section I adopted the UV-optical pseudo-colour $C_{F336W,F438W,F814W}$, analogous to the index $C_{U,B,I}$, which traces the stellar content of N, C, He, and calculated the width of the RGB in the pseudo-CMD $C_{F336W,F438W,F814W}$ vs. m_{F814W} to compare it with some properties of the cluster. Indeed the spread of the RGB sequence in this pseudo-colour is proportional to the variation of the chemical content among the multiple populations that compose the branch.

The procedure is the following, referred to figure 3.10. I identified the m_{F814W} magnitude of the turn-off point ($m_{F814W, TO}$=18.6, blue dashed line) and considered the RGB width at 2 magnitudes above (m_{F814W}=16.6, blue solid line). At this height I computed the 4th and the 96th percentiles (green points) of the distribution in the pseudo-colour, then the RGB width was calculated as the difference between the $C_{F336W,F438W,F814W}$ value in these points. Finally the error was given by the 68.27th percentile of the errors distribution. The obtained result was:

$$W^{RGB}_{F336W,F438W,F814W} = 0.233 \pm 0.029$$

To further investigate the meaning of this result relative to other globular clusters studied in literature, I sourced from the paper of Lagioia et al. 2019 two figures where the relation between $W^{RGB}_{F336W,F438W,F814W}$ with the metallicity and the cluster mass alternatively are shown. The sample of Lagioia et al. presented in these images included 58 Galactic globular clusters.

In figure 3.11 there is the scatter plot of $W^{RGB}_{F336W,F438W,F814W}$ vs. [Fe/H], with the vertical errorbar that represents the error of the RGB width measurement. The green point is the one I inserted, basing on the obtained RGB width and a mean metallicity of NGC 6273 assumed as [Fe/H] = –1.61 dex (Johnson et al. 2017). The dimension of the plotted points is proportional to the mass of the corresponding cluster, and for this proportionality I used a value of log(M/M$_\odot$) = 6.08 (M ~ 1.2×10^6 M$_\odot$, Brown et al. 2010). Metallicity is the most important physical parameter impacting the extension of the RGB width (Lagioia et al. 2019), which results to be a sensitive

indicator of the total internal chemical variations in clusters. and from the diagram it is evident that this width increases with metallicity. We notice also a slightly linear trend of the points, with a relevant deviation from linearity in the range $-1.7 \lesssim$ [Fe/H] $\lesssim -1.1$, where also the added green point places. This interval coincides with a bigger dimension of the points, indicating that the scatter increases with the mass of the cluster.

The diagrams that follow (figure 3.12) are indeed relative to the cluster mass. The points with the green contour in both panels are the ones I inserted, basing on the aforementioned values of $W_{F336W,F438W,F814W}^{RGB}$, $\log(M/M_\odot)$ and [Fe/H] as ordinate, abscissa and colour of the point, respectively. The top panel displays the scatter plot between the RGB width and the cluster mass, expressed in logarithmic units. Using these three dimensions, we can clearly see that the points are almost arranged along bands of different metallicities, with the metal-rich and metal-poor corresponding to the highest and lowest values of the RGB width, respectively. This result confirms that the metallicity has a predominant role on the characteristics observed in the trend of the RGB width.

In the bottom panel the quantities are the same but the RGB width is expressed as "normalized", $\Delta W_{F336W,F438W,F814W}^{RGB}$, that is the $W_{F336W,F438W,F814W}^{RGB}$ minus the residual with respect to the regression line of figure 3.11. This way the contribution of metallicity is removed from the RGB width of all the considered clusters, giving as result that all points draw a monotonically increasing correlation.

This fact demonstrates that the normalized RGB width is strongly dependent on the mass of the cluster, suggesting that the cluster mass is the main factor affecting the properties of MPs, parametrized by the quantity $\Delta W_{F336W,F438W,F814W}^{RGB}$.
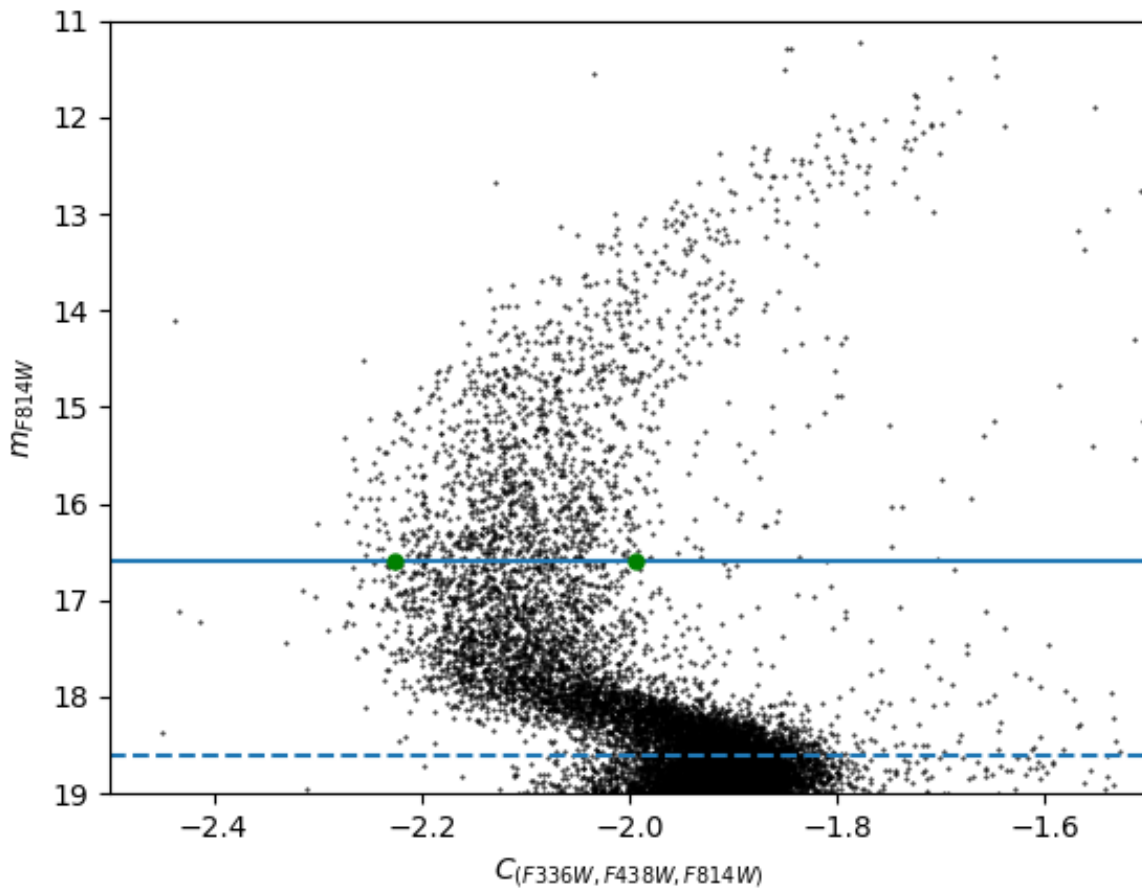
Figure 3.10 Pseudo-colour diagram $C_{F336W,F438W,F814W}$ vs. m_{F814W} with RGB width measurement sketched. Blue dashed line marks the turn-off magnitude, blue solid line is 2 magnitudes above: here the RGB width is calculated. Green points mark the 4th and the 96th percentiles of the pseudo-colour distribution.
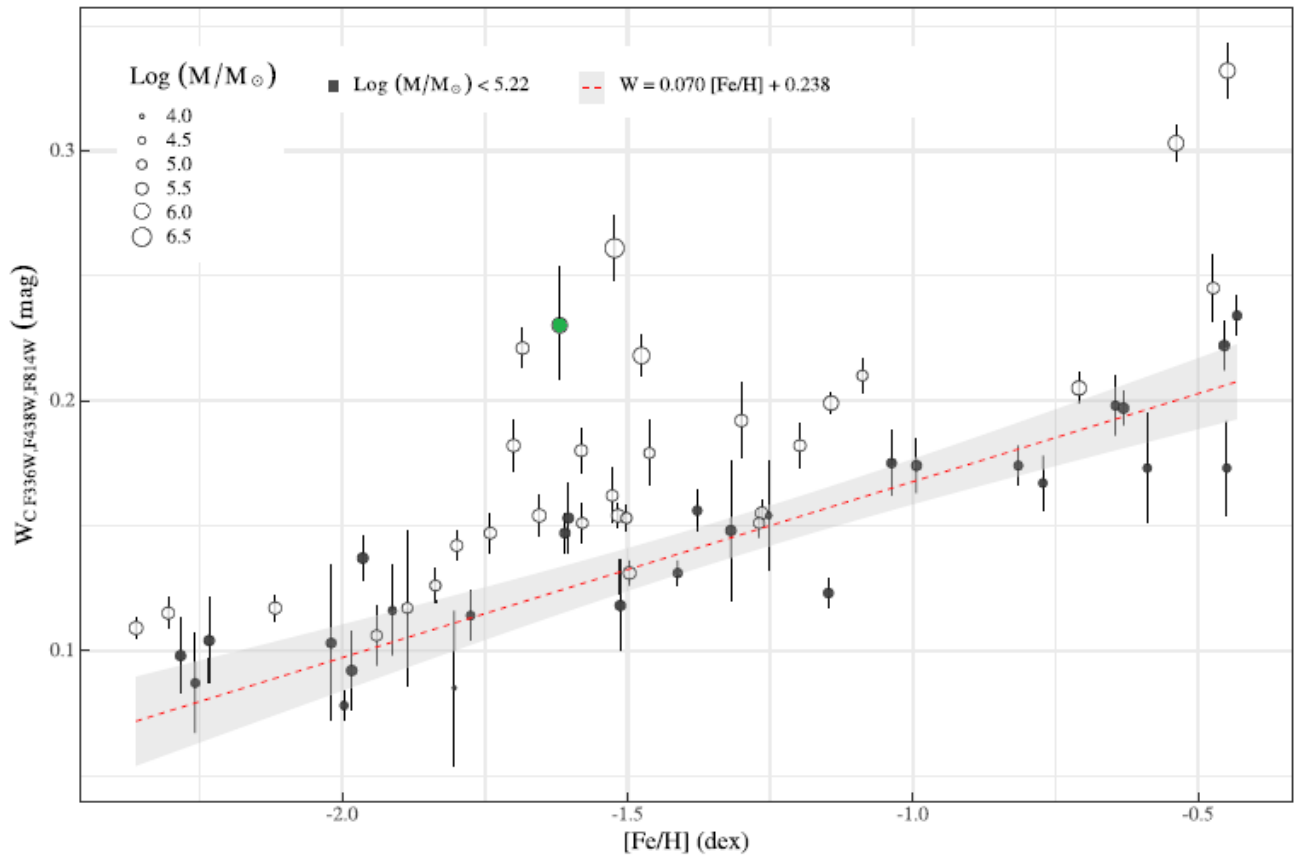
Figure 3.11 Scatter plot of RGB width $W_{F336W,F438W,F814W}$ vs. [Fe/H] for 58 Galactic GCs taken from Lagioia et al. 2019. The point in green was added in this work and is that relative to NGC 6273. The dimension of each point is proportional to the mass of the corresponding cluster. The red dashed line is the linear relation fitting the clusters with log(M/M$_\odot$)<5.22, marked by the black filled points. The gray shaded area marks the 95% confidence interval of the true regression line (Lagioia et al. 2019).
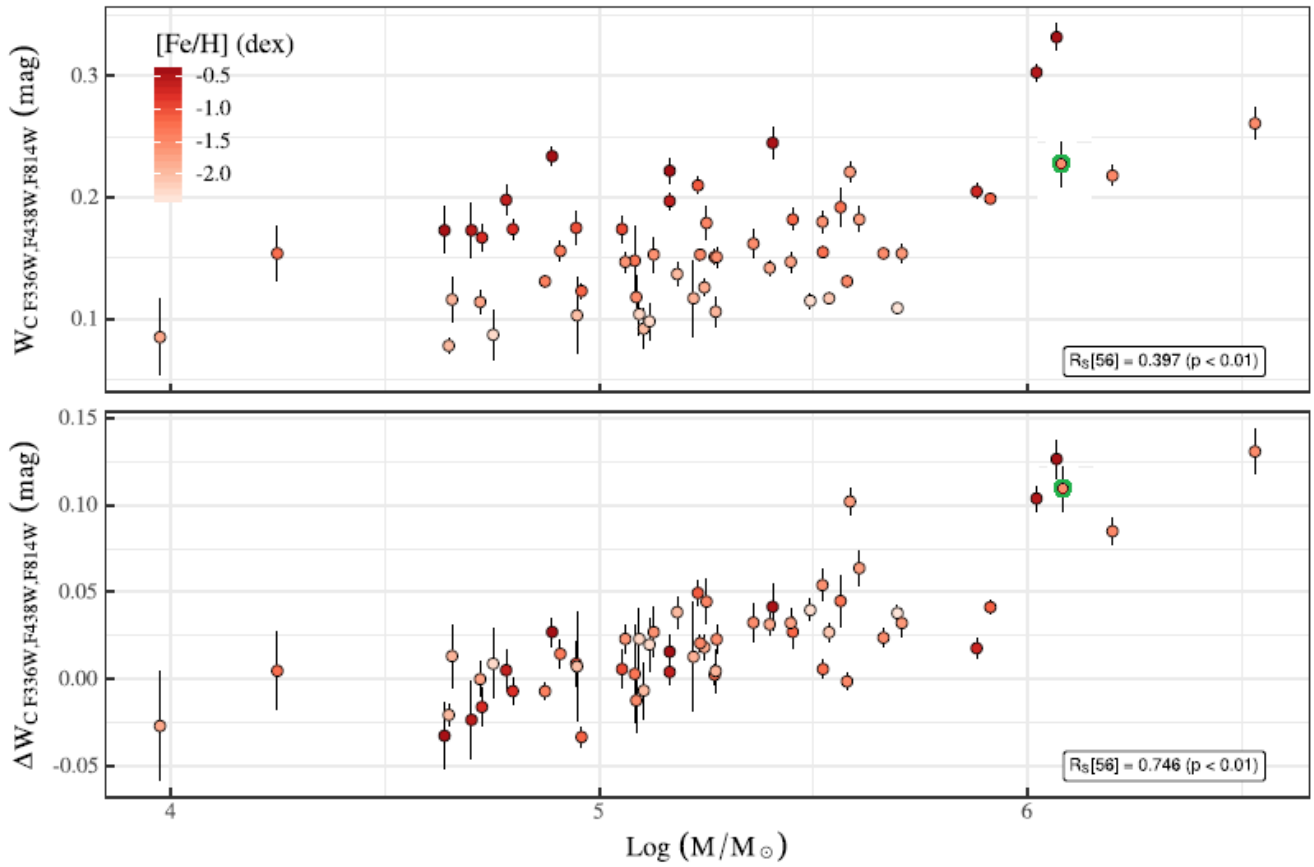
Figure 3.12 Scatter plots of RGB width $W_{F336W,F438W,F814W}$ vs. log(M/M$_\odot$) (top panel) and normalized RGB width $\Delta W_{F336W,F438W,F814W}$ vs log(M/M$_\odot$) (bottom panel) for 58 Galactic GCs taken from Lagioia et al. 2019. The points with the green contour were added in this work and are those relative to NGC 6273. The colour of each point corresponds to the metallicity of the cluster according to the scale in the legend (Lagioia et al. 2019).

3.4 Identification of multiple populations along the AGB

To accomplish the successive analysis on the distribution of AGB stars in type II globular clusters, I constructed some specific colour-magnitude diagrams to perform the identification of these stars. The starting point is to consider that both in a simple population and in two populations with different metallicities, AGB stars are bluer and more luminous than RGB ones, as highlighted in the B–V vs. V CMD of figure 3.4. However in optical CMDs, such as the V–I vs. V of figure 3.5, given that the variations of effective temperature between stars correspond to colour differences, at the high luminosities characteristic of red giant and asymptotic giant branches the typical random photometric errors are of the order of the colour gaps corresponding to the small temperature differences between AGB and RGB stars. This makes the two evolutionary sequences hardly distinguishable and causes the populations with different metallicities to overlap. For this reason it is quite complex to identify stars at different evolutionary stages and in different populations using only optical bands. On the contrary, since the flux in the UV of EAGB stars is significantly higher than the one of RGB stars at similar luminosities, these two sequences show to be well distinguishable in UV-optical CMDs.

The following analysis is based on the initial identification of AGB stars in the optical CMD m_{F555W}–m_{F814W} vs. m_{F814W} where the AGB sequences of all the cluster stellar populations are located in the same region, thus the metal-rich and the metal-poor stars are mixed. Figure 3.13 shows the diagram with a zoom on the upper part ($m_{F814W} < 15.5$), and the red line is the attempt I did by eye to separate AGB stars on the left from RGB stars on the right.

Secondly I employed the UV-optical CMD m_{F336W}–m_{F814W} vs. m_{F336W} to check where the stars previously selected would distribute. This diagram is indeed an efficient tool to separate RGB stars from AGB ones since the latter are placed at brighter F336W magnitudes with respect to the former at similar colours. This is shown in figure 3.14, where the three red segments separate the RGB on the right, the AGB in the middle and the HB on the left. This separation was done by eye too.

In addition, the m_{F336W}–m_{F814W} vs. m_{F336W} CMD allows to separate also populations with different metallicities, and we can see this property in figure 3.15 where the two RGB sequences corresponding to metal-rich (red) and metal-poor (black) populations lie separately and do not mix one with each other.
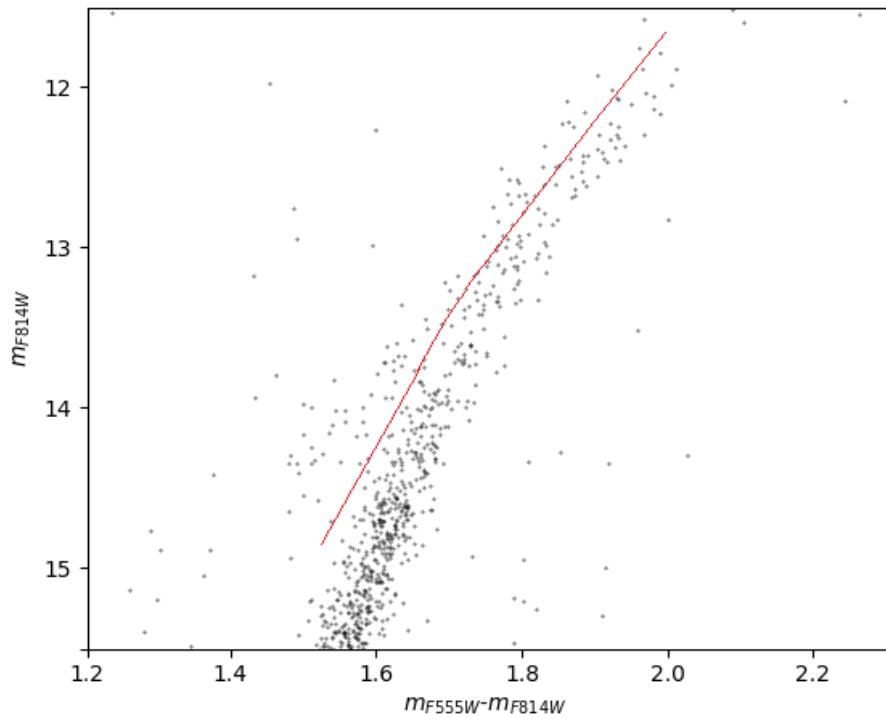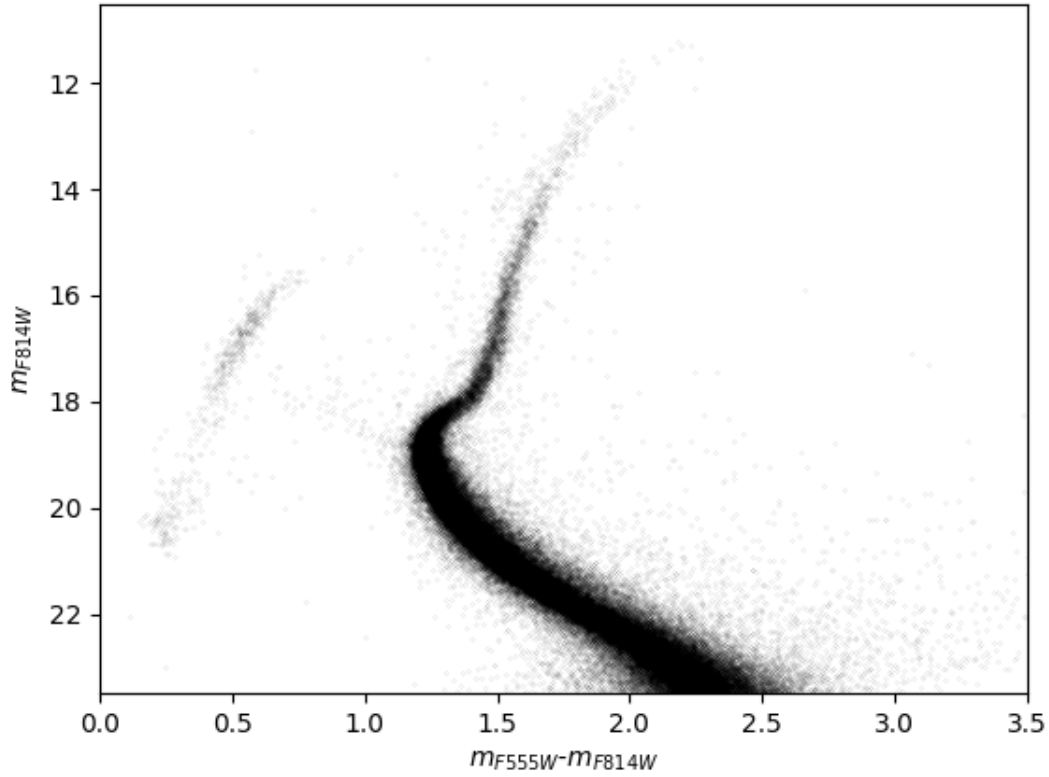
Figure 3.13 m_{F555W}–m_{F814W} vs. m_{F814W} CMD (top) with zoom on the upper part from m_{F814W}<15.5 (bottom) where the red line separates the AGB, on its left, from the RGB, on its right. Separation was done by hand.
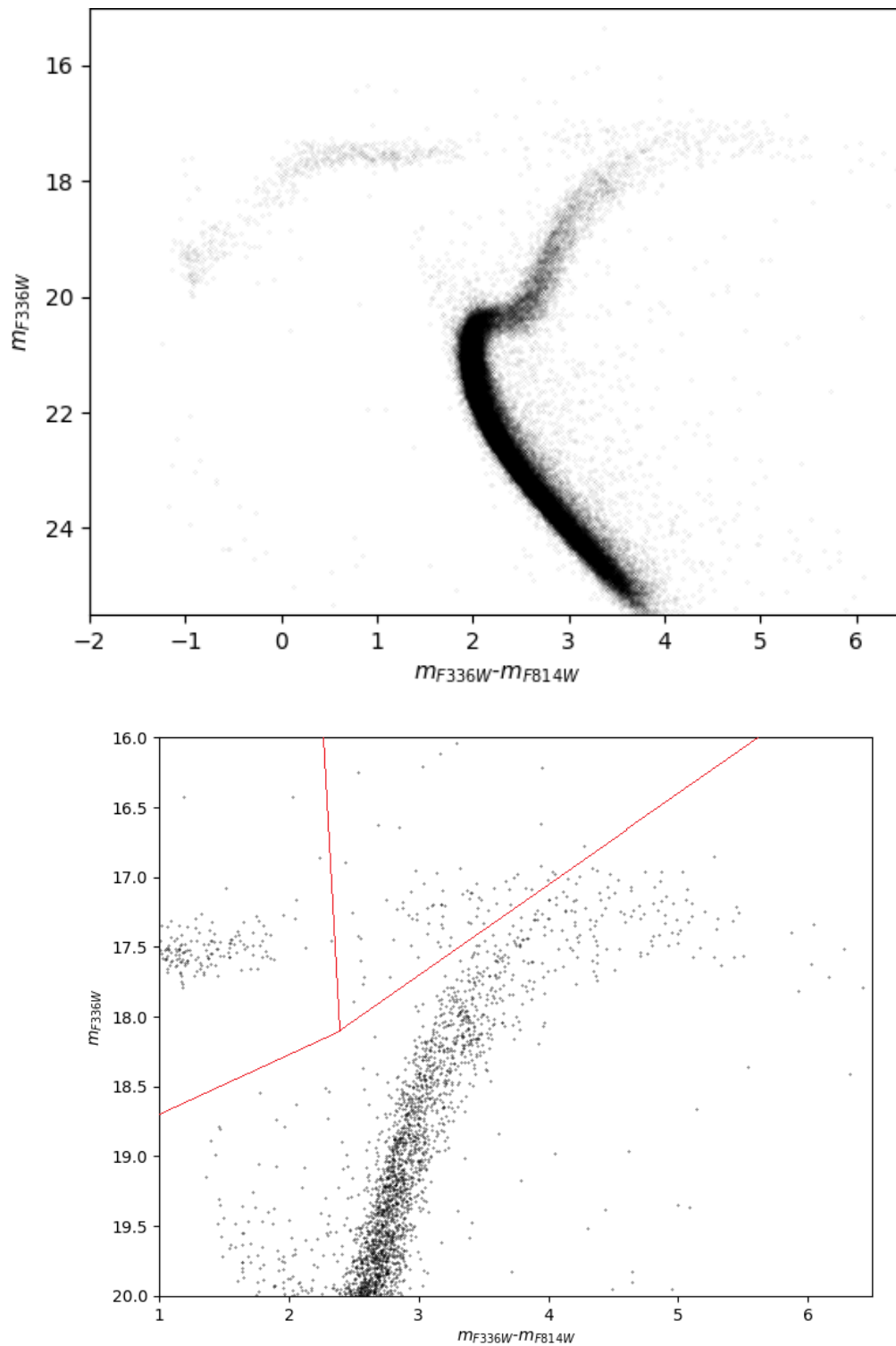
Figure 3.14 m_{F336W}–m_{F814W} vs. m_{F336W} CMD (top) with zoom on the upper part from m_{F336W}<20 (bottom) where red lines separate the RGB, on the right, the AGB, in the middle, and the HB, on the left. Separation was done by hand.
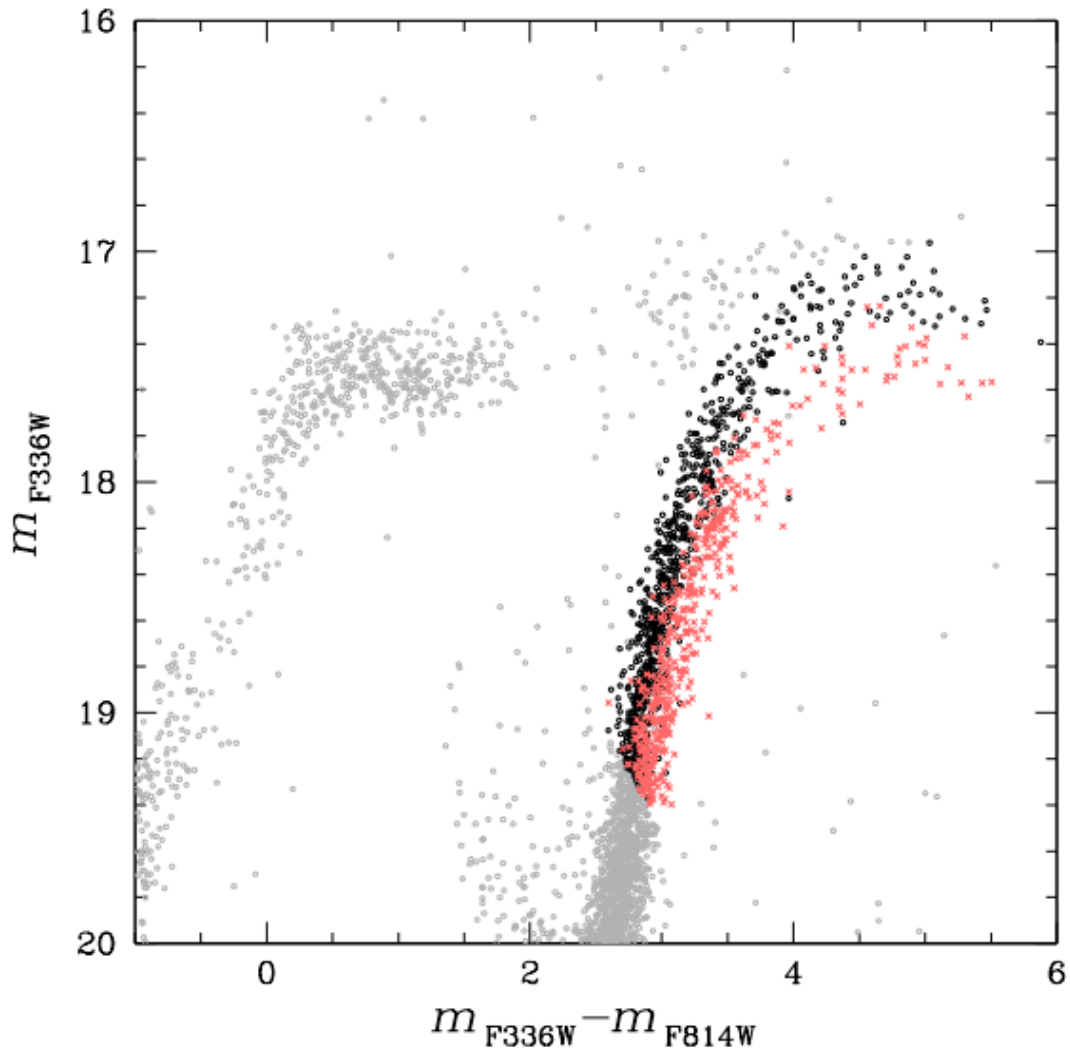
Figure 3.15 Same of bottom panel of figure 3.14 with the two populations identified in figure 3.9 which clearly lie on distinct sequences. Red dots on the right are the metal-rich population, black dots on the left are the metal-poor population.

Having performed a possible identification of AGB candidates, I proceeded from the zoom of figure 3.13 selecting only the points above the red line which show to be the most probable members of the asymptotic branch, for which I chose those lying between $1.5 < m_{F555W} - m_{F814W} < 1.7$ and $13 < m_{F814W} < 15$, that in figure 3.16 are coloured red.
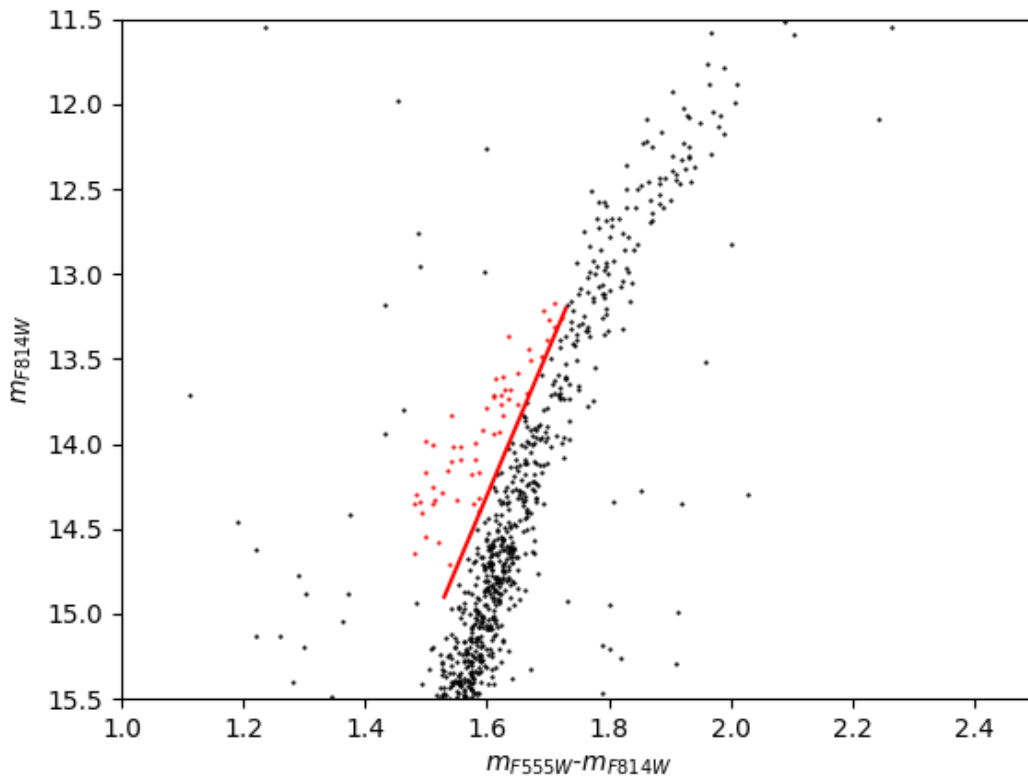
Figure 3.16 Same of bottom panel of figure 3.13 with selected AGB members in red.

The AGB stars selected with these criteria were then highlighted in red in the correspondent UV-optical diagram to check their distribution. The result is shown in figure 3.17, where we can see a bunch of red dots placed in the region identified in figure 3.14 between the RGB and the HB and few red points marked by star symbols that intersect the RGB sequence. These latter are likely to belong to the AGB metal-rich (anomalous) population of our type II globular cluster NGC 6273.
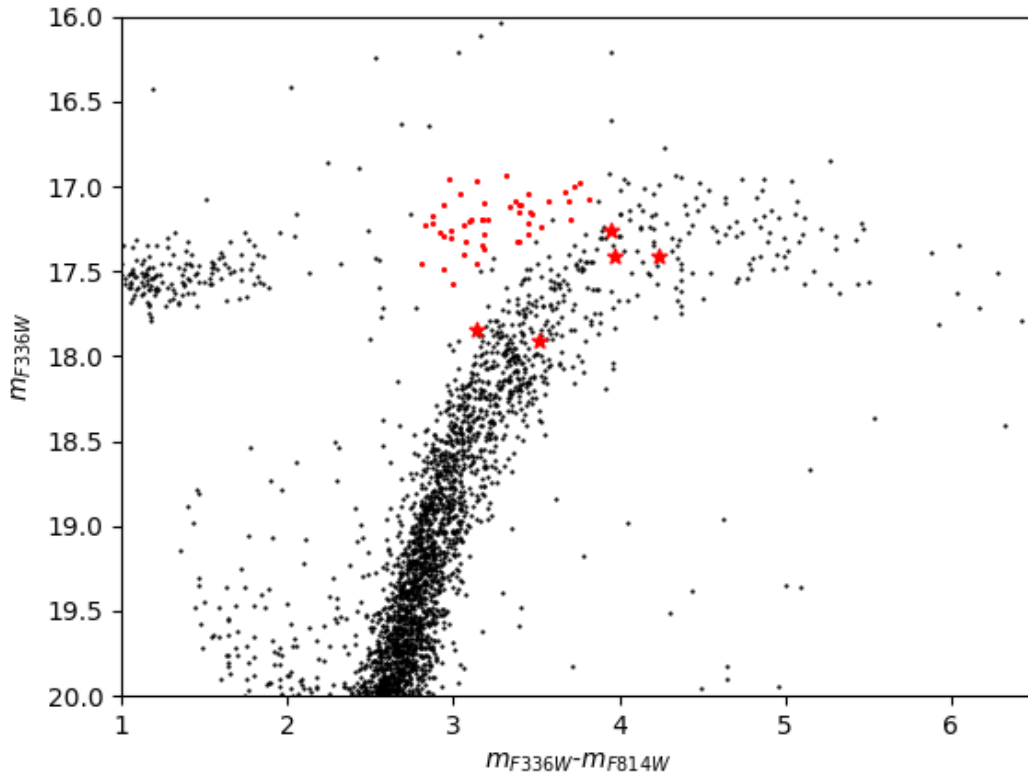
Figure 3.17 Same of bottom panel of figure 3.14 with AGB members in red
and anomalous AGB as star symbols.

The total number of AGB members considered in this procedure was 53 stars, of which 5 resulted to be anomalous stars. Hence the percentage of AGB metal-rich stars is $9 \pm 4\%$, a value that is strikingly lower than the $40 \pm 2\%$ found for the RGB metal-rich population.

This result reveals that NGC 6273 presents a lack of anomalous AGB stars, which is consistent with the AGB manqué scenario where a significant fraction of 2P stars, being enhanced in helium, do not evolve to the AGB because they lose more mass in the RGB phase with respect to 1P stars, leaving HB stars characterized by envelope masses too low to proceed towards the progressive expansion and cooling as normal AGB stars, but rather evolve to higher temperatures until reaching the white dwarf stage.

4. Summary and conclusions

Thanks to the entry into operation of the Hubble Space Telescope with its high photometric qualities, starting from the 1990s the studies of globular clusters have highlighted how they are composed of more than one stellar population, characterized by different chemical properties. In particular the multiple stellar populations phenomenon can be attributed to the presence of two main populations. The so called "primordial population" or "1P" consists of stars having a chemical composition typical of halo stars of the same metallicity, while the other group of stars has a higher abundance mainly of N, Na, He and is called "enriched population" or "2P". Investigated through high-precision photometry, the majority of globular clusters (type I) displays its stars differentiated into these two main stellar populations. However a smaller number of GCs, named type II or anomalous, analyzed also through spectroscopy, shows internal variations not only in the light elements involved in hot H-burning processes and defining the 1P and the 2P, but also in heavier elements, namely those produced via slow neutron-capture reactions. Moreover, recent results added the observed lack of 2P members among AGB stars, as predicted by the AGB manqué scenario in which the stars that are most enriched in helium possess envelope masses too low in the horizontal branch phase, such that they do not evolve as normal asymptotic giant stars but towards higher temperatures until they reach the cooling sequence of the white dwarfs.

In this thesis I focused on the type II Galactic globular cluster NGC 6273 to examine the presence of multiple populations of stars and in particular the presence of members of the anomalous population along the asymptotic giant branch.

I began, as required from the standard procedure, from the reduction of my data composed of a set of images taken in the F336W, F438W, F555W, F814W filters on board the HST. Once obtained the scientific frames reduced and calibrated, I needed to correct them for differential reddening because NGC 6273 is highly affected by this phenomenon, with a colour excess of $\Delta E(B{-}V) = 0.38$, as estimated in this work. With the resulting photometric catalog I then constructed the colour-magnitude diagrams. From a comparison between an original and a corrected for differential reddening CMD I could verify the entity of the spatially-variable extinction since the former appears to be larger than the latter even by a factor of two, particularly nearby the turn-off point.

Therefore with the corrected data I could extract combinations of optical and UV CMDs. The diagrams constructed with purely optical bands, namely F555W and F814W, exhibit evolutionary sequences that are too narrow to distinguish the phenomenon of multiple populations but are ideal to recognize the various evolutionary stages, while combining optical with UV bands, in my case F438W and F336W, we obtain photometric diagrams where the separation in colour of the points is larger, so that we can appreciate the different sequences of points belonging to different stellar populations.

The spread in colour, even once considered the photometric errors, is in fact remarkable for example in the red giant branch in the pseudo-CMD $C_{F438W,F555W,F814W}$, sensitive to populations with different metallicities. Moreover, the chromosome map is a useful tool to maximize the separation of populations with different chemical composition, so that employing the $\Delta_{C\_F438W,F555W,F814W}$ vs. $\Delta_{F336W,F438W}$ ChM I found two distinct populations in the RGB, with the metal-rich one comprising the $40 \pm 2\%$ of the total number of RGB stars.

The width of the red giant branch is indeed an important parameter used to quantify and compare the extent of MPs in various clusters. To perform this calculation I considered the magnitude of the RGB in the pseudo-CMD $C_{F336W,F438W,F814W}$ vs. m_{F814W} at two units above the turn-off point and took the distance between the 4th and the 96th percentiles of the $\Delta C_{F336W,F438W,F814W}$ distribution. Then I compared the value obtained with RGB widths of GCs already present in literature, sourced from Lagioia et al. 2019, taking as reference three relations. The first showed the RGB width versus the metallicity of the cluster, for which the trend appears to be moderately linear with a prominent scatter in a restricted metallicity interval, where also the point representing NGC 6273 falls. This deviation from linearity results to be linked to massive clusters. The other two were the relation between the cluster mass versus the RGB width and then versus the RGB width normalized, from which emerged that the metallicity has a predominant effect on the observed trend, but once subtracted its contribution what we obtain is a new linear correlation. This implies that the mass of the cluster plays a significant role in the incidence of MPs in globular clusters, with more massive clusters displaying greater metallicity-free RGB width, hence more complex MP phenomenon.

Next, my analysis moved to AGB stars along multiple populations, involving as first step to consider which diagrams to employ in order to identify its members. I initially exploited the optical CMD $m_{F555W}-m_{F814W}$ vs. m_{F814W} to separate AGB points from RGB ones, and taking into consideration only those points that have the highest probability to belong to the AGB sequence I checked their position in the $m_{F336W}-m_{F814W}$ vs. m_{F336W} CMD. In this diagram the evolutionary sequences are

larger, so that I could verify the placement of the anomalous population of AGB stars which results to have higher magnitudes with respect to normal AGB stars at the same colours, thus intersecting the RGB sequence. Finally, a quantitative evaluation showed that only the $9 \pm 4\%$ of the total number of the selected AGB stars proved to belong to the metal-rich or anomalous population, with a remarkable the discrepancy between this percentage and the one relative to the RGB anomalous population.

The important evidence of this process of identification is that NGC 6273, similarly to other type II GCs where the anomalous AGB populations have been studied (e. g. Lagioia et al. 2021), exhibits a shortage of anomalous AGB members, namely those stars containing higher abundances of elements heavier than iron which are produced via slow neutron capture process, these reactions being characteristic of the AGB phase. The explanation of this fact is connected to the extreme helium content of these stars, which implies that during the RGB phase they suffer violent mass loss due to stellar winds thus leaving HB stars with tiny hydrogen envelopes. This condition hinders the successive evolution to the early AGB stadium in which the outer envelope contracts and then expands, in response to the changings happening in the layers below. Hence all the successive processes typical of AGB stars, including the rich nucleosynthesis happening in the episodes of dredge-up, are avoided, and the horizontal branch stars move directly towards the stadium of white dwarf. Results on NGC 6273 suggest that most metal-rich stars avoid the AGB phase, thus evolving as AGB manqué stars.

Bibliography

A. F. Marino, A. P. Milone, A. Renzini et al., *Spectroscopy and photometry of the least massive type II Globular Clusters: NGC 1261 and NGC 6934*, The Astrophysical Journal 923:22, Dec 2021.

A. F. Marino, D. Yong, A. P. Milone et al., *Metallicity variations in the type II Globular Cluster NGC 6934*, The Astrophysical Journal 859:81, Jun 2018.

A. F. Marino, A. P. Milone, A. I. Karakas et al., *Iron and s-elements abundance variations in NGC 5286: comparison with anomalous globular clusters and Milky Way satellites*, Monthly Notices of the Royal Astronomical Society, vol. 450, issue 1, Jun 2015.

A. F. Marino, A. P. Milone, G. Piotto et al., *A double stellar generation in the globular cluster NGC 6656 (M22)*, Astronomy&Astrophysics 505, May 2009.

A. P. Milone, G. Cordoni, A. F. Marino et al., *Hubble Space Telescope survey of Magellanic Cloud star clusters. Photometry and astrometry of 113 clusters and early results*, Astronomy&Astrophysics 672, Apr 2023.

A. P. Milone, A. F. Marino, *Multiple Populations in Star Clusters*, Universe 2022, vol. 8, issue 7, Jun 2022.

A. P. Milone, G. Piotto, A. Renzini et al., *The Hubble Space Telescope UV Legacy Survey of Galactic globular clusters – IX. The Atlas of multiple stellar populations*, Monthly Notices of the Royal Astronomical Society, vol. 464, issue 3, Jan 2017.

A. P. Milone, G. Piotto, L. R. Bedin et al., *The ACS survey of Galactic globular clusters. XII. Photometric binaries along the amin sequence*, Astronomy&Astrophysics 540, 2012.

A. P. Milone, L. R. Bedin, G. Piotto et al., *The ACS survey of Galactic globular clusters. III. The double subgiant branch of NGC 1851*, The Astrophysical Journal 673:241, Jan 2008.

E. P. Lagioia, A. P. Milone, A. F. Marino et al., *Multiple Stellar Populations in Asymptotic Giant Branch Stars of Galactic Globular Clusters*, The Astrophysical Journal 910:6, Mar 2021.

E. P. Lagioia, A. P. Milone, A. F. Marino et al., *The role of cluster mass in the multiple populations of galactic and extragalactic globular clusters*, The Astronomical Journal 158:202, Nov 2019.

E. P. Lagioia, A. P. Milone, A. F. Marino et al., *The Hubble Space Telescope UV Legacy Survey of Galactic globular clusters – XII. The RGB bumps of multiple stellar populations*, Monthly Notices of the Royal Astronomical Society, vol. 475, issue 3, Apr 2018.

C. Bonatto, F. Campos, K. S. Oliveira, *Mapping the differential reddening in globular clusters*, arXiv:1307.3935 [astro-ph.GA], Jul 2013.

E. Carretta, A. Bragaglia, R. Gratton et al., *Na-O anticorrelation and HB. VII. The chemical composition of first and second-generation stars in 15 globular clusters from GIRAFFE spectra*, Astronomy&Atrophysics 505, May 2009.

E. Carretta, A. Bragaglia, R. Gratton et al., *Properties of stellar generations in globular clusters and relations with global parameters*, Astronomy&Astrophysics 516, Mar 2010.

R. Gratton, A. Bragaglia, E. Carretta et al. *What is a globular cluster? An observational perspective*, The Astronomy and Astrophysics Review 27:8, Nov 2019.

A. Bragaglia, E. Carretta, R. Gratton et al., *Helium in first and second-generation stars in globular clusters from spectroscopy of red giants*, Astronomy&Astrophysics 519, May 2010.

G. Piotto, A. P. Milone, J. Anderson et al., *Hubble Space Telescope reveals multiple subgiant branch in eight globular clusters*, The Astrophysical Journal 760:39, Nov 2012.

G. Piotto, M. Zoccali, I. R. King et al., *Hubble Space Telescope observations of Galactic globular clister cores. II. NGC 6273 and the problem of horizontal branch gaps*, The Astronomical Journal 118:1727, Oct 1999.

G. A. Rutledge, J. E. Hesser, P. B. Stetson et al., *Galactic globular cluster metallicity scale from the Ca II triplet I. Catalog*, Publications of the Astronomical Society of the Pacific 109:883, Aug 1997.

C. I. Johnson, R. M. Rich, C. A. Pilachowski et al., *A spectroscopic analysis of the Galactic Globular Cluster NGC 6273 (M19)*, arXiv:1507.00756 [astro-ph.SR], Jul 2015.

C. I. Johnson, N. Caldwell, R. M. Rich et al., *A chemical composition survey of the iron-complex globular cluster NGC 6273 (M19)*, The Astrophysical Journal 836:168, Feb 2017.

A. C. Layden, A. Sarajedini, *Photometry of the globular cluster M54 and the Sagittarius dwarf galaxy: the age-metallicity relation*, The Astronomical Journal 119:1760, Apr 2000.

F. D'Antona, E. Vesperini, A. D'Ercole et al., *A single model for the variety of multiple-population formation(s) in globular clusters: a temporal sequence*, Monthly Notices of the Royal Astronomical Society, vol. 458, issue 2, May 2016.

T. Decressin, G. Meynet, C. Charbonnel et al, *Fast rotating massive stars and the origin of the abundance patterns in galactic globular clusters*, Astronomy&Astrophysics 464, 2007.

S. E. de Mink, O. R. Pols, N. Langer, R. G. Izzard, *Massive binaries as the source of abundance anomalies in globular clusters*, Astronomy&Astrophysics 507, Oct 2009.

J. Alonso-Garcìa, M. Mateo, B. Sen et al., *Uncloaking globular clusters in the inner Galaxy*, The Astronomical Journal 143:70, Mar 2012.

E. W. Olszewski, A. Saha, P. Knezek et al., *A 500 parsec halo surrounding the galactic globular NGC 1851*, The Astronomical Journal 138:1570, Dec 2009.

N. Bastian, C. Lardo, *Multiple Stellar Populations in Globular Clusters*, arXiv:1712.01286v1 [astro-ph.SR], Dec 2017.

N. Bastian, H. J. G. Lamers, S. E. de Mink et al., *Early disc accretion as the origin of abundance anomalies in globular clusters*, Monthly Notices of the Royal Astronomical Society, vol. 436, issue 3, Dec 2013.

A. Dotter, A. Sarajedini, J. Anderson et al., *The ACS survey of Galactic globular clusters. IX. Horizontal Branch morphology and the second parameter phenomenon*, The Astrophysical Journal 708:698, Jan 2010.

D. A. Vandenberg, T. M. Brown, J. Tumlinson et al., *The quenching of the ultra-faint dwarf galaxies in the reionization era*, The Astrophysical Journal 796:91, Dec 2014.

P. A. Denissenkov, F. D. A. Hartwick, *Supermassive stars as a source of abundance anomalies of proton-capture elements in globular clusters*, Monthly Notices of the Royal Astronomical Society, vol. 437, issue 1, Oct 2013.

A. Renzini, A. Buzzoni, *Spectral evolution of galaxies*, 1986.

A. Renzini, F. D'Antona, S. Cassisi et al., *The Hubble Space Telescope UV legavy survey of Galactic globular clusters – V. Constraints on formation scenarios*, Monthly Notices of the Royal Astronomical Society, vol. 454, issue 4, Dec 2015.

A. Renzini, *Finding forming globular clusters at high redshifts*, Monthly Notices of the Royal Astronomical Society, vol. 469, issue 1, Jul 2017.

M. Gieles, C. Charbonnel, M. G. Krause et al., *Concurrent formation of supermassive stars and globular clusters: implications for early self-enrichment*, Monthly Notices of the Royal Astronomical Society, vol. 478, issue 2, Aug 2018.

T. M. Brown, A. V. Sweigart, T. Lanz et al., *The blue hook populations of massive globular clusters*, The Astrophysical Journal 718:1332, Aug 2010.

D. I. Casetti-Dinescu, T. M. Girard, V. I. Korchagin et al., *Space velocities of southern globular clusters. VI. Nine clusters in the inner Milky Way*, The Astronomical Journal 140:1282 Nov 2010.

P. Marigo, dispense di Astrofisica 2, capitolo 11, *Late evolution of low- and intermediate-mass stars*, a. a. 2019 – 2020.